Title (120 characters):

Selective clearance of the inner nuclear membrane protein emerin by vesicular transport during ER stress

Authors: Abigail Buchwalter[1,2,3]*, Roberta Schulte[4], Hsiao Tsai[4], Juliana Capitanio[4], and Martin Hetzer[4]*

[1]Cardiovascular Research Institute, University of California San Francisco, San Francisco, CA, USA

[2]Department of Physiology, University of California San Francisco, San Francisco, CA, USA

[3]Chan Zuckerberg Biohub, San Francisco, CA, USA

[4]The Salk Institute for Biological Studies, La Jolla, CA, USA

*corresponding authors

Abstract

Proteins of the inner nuclear membrane (INM) participate in nuclear positioning and genome organization. The INM is a subdomain of the endoplasmic reticulum (ER) that is gated by the nuclear pore complex. It is unknown whether proteins of the INM and ER are degraded through shared or distinct pathways in mammalian cells. We applied dynamic proteomics to profile protein half-lives and report that INM and ER residents turn over at similar rates, indicating that the INM's unique topology is not a barrier to turnover. By imaging the INM protein emerin, we observed that the proteasome can degrade INM proteins *in situ*. However, we also uncovered evidence for selective, vesicular transport-mediated turnover during ER stress. Emerin is rapidly cleared from the INM by a mechanism that requires emerin's LEM domain to mediate vesicular trafficking to lysosomes. This work demonstrates that the INM can be dynamically remodeled in response to environmental inputs.

Introduction

The biogenesis of roughly one-third of the cell's proteome takes place within the endoplasmic reticulum (ER) network. Ribosomes associated with translocon channels feed nascent proteins into the ER. The lumen of the ER is enriched with folding chaperones that promote the effective maturation of newly synthesized proteins.

The ER is contiguous with the nuclear envelope (NE) membrane, a double bilayer membrane that defines the boundary of the nucleus. The NE is punctuated by nuclear pore complexes (NPCs) which control transport between the nuclear and cytoplasmic compartments. The outer nuclear membrane (ONM) and the bulk ER membrane network have a similar protein composition, including ribosomes that can be seen associated with the ONM. The inner nuclear membrane (INM), in contrast, is cloistered away from the bulk ER network by the NPC (Fig. 1A). Proteomic analyses suggest that hundreds of proteins are selectively concentrated at the INM(Schirmer, Florens, Guan, Yates, & Gerace, 2003). Mutations to INM proteins cause a broad array of rare pathologies(Schreiber & Kennedy, 2013).

As the INM is devoid of ribosomes and translocation machinery, INM proteins must be synthesized in the ONM/ER and transported into the INM. Proteins concentrate at the INM by mechanisms including diffusion followed by stable binding to a nuclear structure, such as chromatin or the nuclear lamina, or signal-mediated import through the NPC(Katta, Smoyer, & Jaspersen, 2014). Transport across the NPC is a major kinetic barrier to accumulation of proteins at the INM(Boni et al., 2015; Ungricht, Klann, Horvath, & Kutay, 2015). While mechanisms of INM targeting have been extensively studied, it is less clear how INM proteins are targeted for degradation if misfolded, damaged, or mistargeted.

Protein folding is inefficient, and newly synthesized proteins often become terminally misfolded and require degradation(Hegde & Zavodszky, 2019). Mature proteins may also become damaged or misfolded over time and require selective degradation and replacement. Within the ER membrane network, the major degradation pathway is ER-associated degradation, or ERAD. ERAD is initiated by poly-ubiquitination of a target protein by an E3 ubiquitin ligase, followed by extraction from the membrane and proteolysis by proteasomes in the cytosol(Hegde & Zavodszky, 2019). Flux through ERAD helps to maintain organelle homeostasis and cell function by clearing damaged, misfolded, or mislocalized proteins.

Recent work in *S. cerevisiae* has identified a small number of ubiquitin ligases that target INM-localized proteins for degradation by ERAD, but the mammalian homologs remain elusive, perhaps because of the massive expansion of the E3 ubiquitin ligase family in recent evolution(Deshaies & Joazeiro, 2009). Degradation of mammalian INM proteins also appears to rely on activity of the proteasome and on the ERAD ATPase p97(Tsai, Zhao, Turner, & Schlieker, 2016), suggesting that mammalian INM proteins may be subject to ERAD. However, we lack a broad understanding of the lifetimes of INM proteins in this compartment and the pathways used for their degradation within mammalian cells.

We sought to understand features of INM protein turnover in mammalian cells, and applied both proteome-wide and targeted candidate approaches to address this question. Here we show that the LEM domain protein emerin (EMD) is a rapidly degraded constituent of the INM. We use EMD as a model for dissecting INM protein turnover pathways and demonstrate that EMD is subject to both proteasome-dependent and vesicular transport-dependent modes of degradation. We report that both misfolded and normally folded variants of EMD are selectively exported from the INM and ER during acute ER stress by vesicular transport. These findings indicate that the INM sub-compartment senses and responds to ER stress.

Results

Trends in protein turnover across the NE / ER membrane network

We first used a dynamic proteomic approach to understand trends in protein turnover across ER sub-compartments. Since the nucleus is entirely disassembled during mitosis in mammalian cells, we chose a system that would allow us to profile protein turnover in the absence of cell division. We made use of the C2C12 myoblast culture system, which can be induced to irreversibly differentiate into myotubes by serum withdrawal(DaposAngelo, Raices, Panowski, & Hetzer, 2009). We subjected these non-dividing mouse muscle myotubes to a pulse-chase timecourse using stable isotope labeling in cell culture (SILAC) (Ong & Mann, 2007) for timepoints ranging from 1 to 3 days (Fig. 1B, see Methods). Crude nuclear extracts were prepared and analyzed by mass spectrometry, and the ratio of “old” ($^{13}C_6$-Lys, $^{15}N_4$ + $^{13}C_6$-Arg-labeled) to “new” ($^{12}C_6$-Lys, $^{14}N_4$ + $^{12}C_6$-Arg-labeled) protein was quantified at the peptide level over time; peptides that passed stringent quality control filters were retained for estimation of half-lives by a linear regression fitting method(Dörrbaum, Kochen, Langer, & Schuman, 2018)(see Methods). We evaluated 1677 proteins and predicted half-lives over a wide range, from less than a day to greater than 15 days (Fig. 1E, Table S3). Linear regression performs well when a line can be fit with high fidelity and a non-zero slope is detectable; these conditions were generally met for proteins with predicted half-lives ranging from 1 to 8 days. We observed more frequent deviations in linearity at the low

extreme (predicted $t^{1/2}$ <1 day) and slopes approaching zero at the high extreme (predicted $t^{1/2}$ > 8 days) (Fig. S1). We expect that these factors limit the precision of half-life determination below 1 day and above 8 days from our 3-day timecourse. The median turnover rate that we observed (2.4 days) corresponds well with previous analyses in non-dividing mammalian cell cultures(Cambridge et al., 2011).

We observed some extremes in protein stability that are consistent with previous reports; for example, the long-lived nuclear pore complex component Nup160(Toyama et al., 2013) was in the top 10% of predicted half-lives, with a calculated half-life of approximately 18 days (Fig. 1C, F, Table S1). Near the other extreme, we observed that the enzyme topoisomerase 2α (Topo2α) had a predicted half-life in the bottom 10%, of less than 1 day (Fig. 1D, F). This is consistent with this enzyme's known regulation by ubiquitination and proteolysis(Gao et al., 2014).

Having established this framework, we then quantified the turnover kinetics of known inner nuclear membrane (INM) proteins. For this analysis, we focused on proteins whose preferential enrichment in this membrane compartment had been experimentally verified; we identified ten such proteins in our dataset (see Table S1) and determined their half-lives (see Methods). We observed half-lives for these proteins ranging from 8.8 days (nurim) to 1.5 days (emerin) (Fig. 1G). While very little is known about nurim's function, its intrinsic biophysical properties may contribute to its long half-life: nurim contains six transmembrane domains, is extremely insoluble(Hofemeister & O'Hare, 2005), and diffuses very slowly within the INM(Rolls et al., 1999). Emerin (EMD) is a founding member of the LEM domain family of INM proteins with essential functions in muscle development(Brachner & Foisner, 2011). Unlike nurim, EMD is a small (~25 kDa), single-pass, tail-anchored transmembrane protein that diffuses freely through the NPC and enriches at the INM by virtue of its affinity for lamin A(Vaughan et al., 2001).

Given the INM's status as a restricted sub-compartment of the ER, we reasoned that it might be possible that INM proteins would be generally less accessible to protein turnover than ER membrane proteins. Alternatively, similarly effective turnover in both

Figure 1. Proteomic analysis of nuclear envelope protein half-lives in C2C12 myotubes.

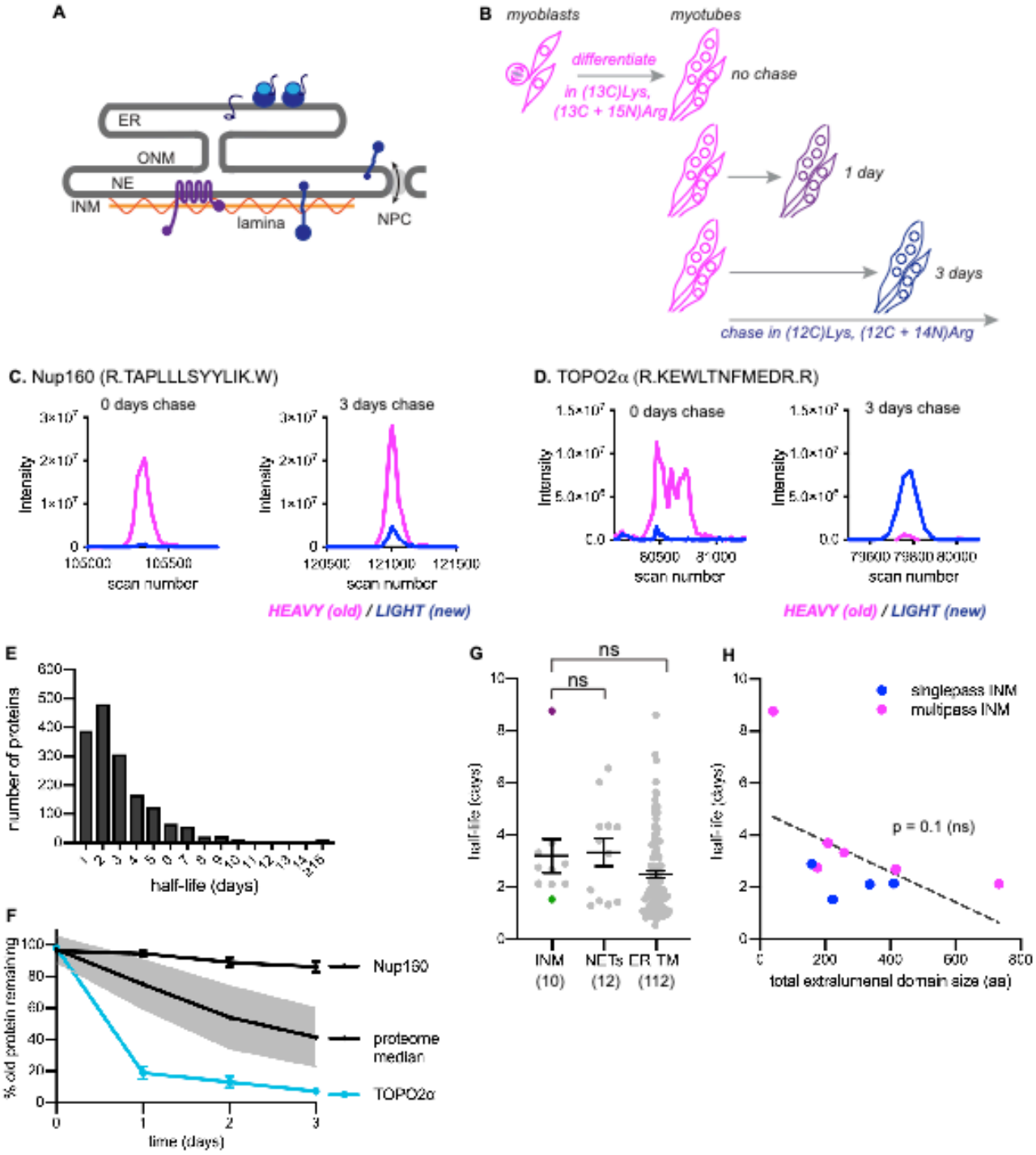

Figure 1. Dynamic proteomic analysis of inner nuclear membrane protein turnover. (A) Diagram of the ER with associated ribosomes, the NE composed of the ONM and INM, the NPCs, and the underlying nuclear lamina. INM proteins are synthesized in the ER, pass through the NPC, and enrich at the INM. (B) Overview of dynamic SILAC labeling experimental design. C2C12 mouse myoblasts were cultured for 5 population doublings in medium containing $^{13}C_6$-lysine and $^{13}C_6$, $^{15}N_4$-arginine to completely label the proteome. After 3 days of culturing under differentiating conditions to generate non-dividing myotubes, cultures were switched to chase medium containing ^{12}C-lysine and ^{12}C, ^{14}N-arginine for 1 to 3 days. Nuclear extracts were prepared at day 0, day 1, day 2, and day 3 for proteomic identification. (C,D) Representative peptide scans for a slowly degraded protein (Nup160) and (D) for a rapidly degraded protein (Topo2α) at the starting and ending points of the experiment outlined in (B). (E) Histogram of calculated half-lives for 1677 proteins with a median half-life of 2.4 days. (F) Features of nuclear proteome turnover. Median turnover behavior of 1677 proteins detected in at least three timepoints with at least one peptide (black line) with 1 standard deviation (gray); compared to turnover of the slowly exchanged protein Nup160 (black) and the rapidly exchanged protein Topo2α (blue). Error bars indicate SEM. (G) Calculated half-lives of 10 *bona fide* INM proteins, ranging from slowly degraded (nurim, purple) to rapidly degraded (emerin, green); 12 nuclear envelope transmembrane proteins (NETs) identified as NE residents by subtractive proteomics (see Schirmer, 2003); and 112 ER membrane proteins. ns indicates lack of statistical significance by Mann-Whitney test. Error bars indicate SEM. (H) There is no significant correlation between extraluminal domain size of INM proteins and their half-lives. See also Tables S1-S5.

compartments might support the possibility that turnover can occur *in situ* at the INM. ER membrane proteins were well represented in our dataset, as a significant proportion of ER membranes remain attached to and co-purify with nuclei(Schirmer et al., 2003). We could thus query whether INM proteins exhibited distinct turnover kinetics from membrane proteins of the bulk ER by comparing INM and ER transmembrane protein half-lives. We also compared *bona fide* INM proteins to proteins that had been identified as preferentially associated with either the inner or outer bilayer of the nuclear envelope (NE) membrane by comparative proteomics(Schirmer et al., 2003), termed NE transmembrane proteins (NETs). Altogether, these analyses indicate that INM proteins do not exhibit unique turnover kinetics as a protein class, compared to ER membrane proteins in general or to the overlapping designation of NETs (Fig. 1G).

The size of INM proteins determines whether a protein must rely on signal-mediated transport through the NPC(Katta et al., 2014), and live imaging assays indicate that INM proteins with larger nucleoplasm-facing domains move more slowly across the NPC barrier(Boni et al., 2015; Ungricht et al., 2015). If transit across the NPC and out of the

158 INM were a prerequisite for turnover in the bulk ER, we reasoned that turnover
159 efficiency would also exhibit some dependence on protein size, because of the
160 relationship between protein size and transport efficiency between the two
161 compartments. The short half-life and small size of EMD is in line with this possibility.
162 Our dataset of INM proteins included four single-pass INM and six multi-pass INM
163 proteins, with total size of extraluminal domains ranging from 40 amino acids to 733
164 amino acids (Table S5). If export out of the NPC were a prerequisite for INM protein
165 turnover, we reasoned that half-life should increase as the bulk of nucleoplasm-facing
166 domains increases. We found no evidence for such a correlation (Fig. 1H). We infer
167 from this analysis that other factors distinct from monomeric protein size regulate
168 protein turnover rate. This indicates that for INM proteins, export out of the INM is not a
169 rate-limiting step for protein turnover. Rather, this is consistent with evidence in *S.*
170 *cerevisiae*(Foresti, Ruggiano, Hannibal-Bach, Ejsing, & Carvalho, 2013; Khmelinskii,
171 Blaszczak, Pantazopoulou, Fischer, Omnus, Le Dez, Brossard, Gunnarsson, Barry,
172 Meurer, Kirrmaier, Boone, Huber, Rabut, Ljungdahl, & Knop, 2014a) and in mammalian
173 cells(Tsai et al., 2016)that turnover of INM proteins can take place *in situ* at the INM.
174

175 **Recombination-induced tag exchange confirms INM protein lifetimes**

176 We observed a wide range of half-lives for INM proteins in our proteomic analyses (Fig.
177 1G), with the polytopic INM protein nurim turning over most slowly and the single-pass
178 INM protein EMD turning over most rapidly. To directly visualize these relative
179 differences in protein stability at the INM, we used recombination-induced tag exchange
180 (RITE) (Toyama et al., 2019; Verzijlbergen et al., 2010) (Fig. 2A) to perform a
181 microscopy-based pulse-chase experiment. We expressed either nurim or EMD in a
182 cassette encoding two C-terminal epitope tags separated by LoxP sites and by a stop
183 codon, such that a protein will be expressed in cells with the first tag immediately
184 downstream of the open reading frame. Upon adenoviral introduction of Cre
185 recombinase, the first tag is removed by recombination and the second tag is positioned
186 immediately downstream of the open reading frame, so that all newly synthesized
187 protein carries the second tag. This enables simultaneous tracking of older and newer
188 pools of protein that were synthesized before and after Cre addition, respectively (Toya

Figure 2. RITE analysis of INM proteins corroborates protein turnover determined by proteomics.

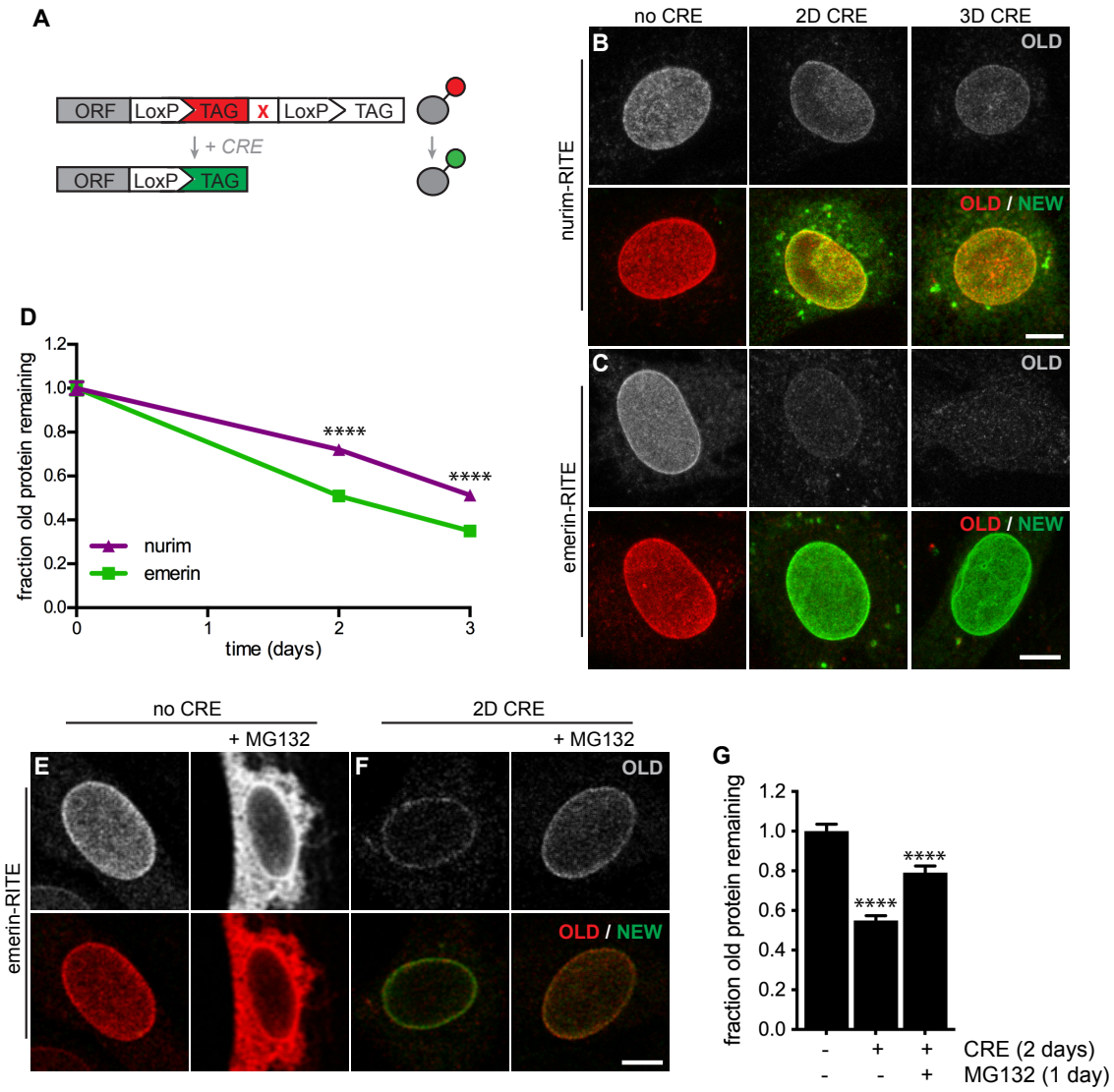

Figure 2. RITE analysis of INM proteins corroborates protein turnover determined by proteomics. (A) Schematic of recombination-induced tag exchange (RITE) expression cassette for visualizing protein turnover. (B-C) RITE timecourses of nurim-RITE (B) and emerin-RITE (C) in quiescent C2C12 cells. (D) Quantification of normalized intensity of old RITE-tagged protein over the timecourses shown in (B-C). Points indicate average values with error bars indicating SEM for N > 153 cells per condition from 2 independent experiments. **** indicates p-value < 0.0001 (by t-test) for comparison between old nurim and emerin levels. (E) Treatment of quiescent C2C12 cells expressing emerin-RITE for 1 day with the proteasome inhibitor MG132. (F) Induction of RITE tag switch by Cre recombinase administration for 2 days (left) or for 1 day followed by Cre and MG132 coincubation for 1 day. (G) Quantification of intensity of old RITE-tagged emerin in the NE across the conditions shown in (E-F). Columns indicate average and error bars indicate SEM for N > 128 cells from

191 ma et al., 2019; Verzijlbergen et al., 2010). Using this approach, we visualized the rate
192 of decline in the fluorescence intensity of “old” myc-tagged nurim or EMD over several
193 days in quiescent C2C12 cells. Consistent with our proteomic observations, we
194 observed that RITE-tagged nurim decayed significantly more slowly than RITE-tagged
195 EMD at the NE (Fig. 2B-D).
196
197 The RITE system allows unambiguous dissection of the fates of maturely folded protein
198 as well as nascent, newly synthesized protein. Recent work in yeast(Foresti et al., 2013;
199 Khmelinskii, Blaszczak, Pantazopoulou, Fischer, Omnus, Le Dez, Brossard,
200 Gunnarsson, Barry, Meurer, Kirrmaier, Boone, Huber, Rabut, Ljungdahl, & Knop,
201 2014a) and in mammalian cells(Tsai et al., 2016) strongly suggests that INM proteins
202 are subject to proteasome-mediated degradation via the ERAD pathway. The RITE
203 system provides a means to distinguish the effects of proteasome inhibition on maturely
204 folded protein and on nascent unfolded or misfolded proteins. When quiescent cells
205 expressing EMD-RITE were subjected to proteasome inhibition by MG132 for 1 day,
206 extensive accumulation of EMD-RITE was observed throughout the NE/ER network
207 (Fig. 2E). Since INM proteins are synthesized in the bulk ER and become enriched at
208 the INM upon proper folding and engagement with binding partners, we infer from this
209 that a proportion of newly synthesized EMD is degraded in a proteasome-dependent
210 manner in the peripheral ER. On the other hand, if proteasome inhibitor was
211 administered after RITE tag switching, a partial stabilization of maturely folded EMD at
212 the NE was observed (Fig. 2F, G). This indicates that mature, INM-localized EMD can
213 be degraded in a proteasome-dependent pathway *in situ* at the INM. Notably, abundant
214 proteasomes have been observed along the INM in cryo-EM studies and could possibly
215 engage with substrate there(Albert et al., 2017). This is also consistent with a recent
216 report that an unstable INM protein mutant accumulates within the nucleus of
217 mammalian cells when the proteasome is inhibited(Tsai et al., 2016).
218
219 **Identification of a model substrate for dissecting INM protein turnover**
220 In order to gain more insight into the pathways that control INM protein turnover in
221 mammalian cells, we chose to focus on EMD for its relatively fast turnover rate (Fig. 1G,

222 Table S1) and for the variety of disease-linked mutations to EMD that appear to
223 influence protein stability(Fairley, Kendrick-Jones, & Ellis, 1999). Loss-of-function
224 mutations to EMD cause Emery-Dreifuss muscular dystrophy (EDMD) (Bonne &
225 Quijano-Roy, 2013). In some cases, EDMD-linked mutations cause loss of detectable
226 EMD protein without affecting mRNA levels, suggesting that these mutations might
227 cause misfolding and degradation of EMD(Fairley et al., 1999). We sought to identify
228 such an EDMD-linked EMD variant for use as a model substrate for dissecting INM
229 protein turnover. We selected a small in-frame deletion (Δ95-99) within EMD's lamin-
230 binding domain (Fig. 3A) that had been previously shown to localize to the NE when
231 ectopically expressed(Fairley et al., 1999). Consistently, when we expressed either
232 EMD or EMDΔ95-99 in C2C12 cells, we observed similar enrichment at the NE (Fig.
233 S2B). Further, both protein variants exhibited residence time at the NE as assayed by
234 fluorescence recovery after photobleaching (FRAP) analysis (Fig. S2). However, when
235 *de novo* protein synthesis was blocked by cycloheximide (CHX), we observed rapid loss
236 of EMDΔ95-99 within 4-8 hours (Fig. 3B, 3D) while wild type EMD remained stable (Fig.
237 3C). These observations indicate that EMDΔ95-99 is an unstable EMD variant that
238 resides within the INM. We next moved to dissect that pathway(s) involved in EMDΔ95-
239 99 degradation.
240
241 **Proteasome-dependent and proteasome-independent modes of emerin clearance**
242 Misfolded ER resident proteins are cleared by the ER-associated degradation (ERAD)
243 pathway. ERAD clients are marked for degradation by ubiquitination, extracted from the
244 ER membrane by the ATPase enzyme p97, and degraded by the proteasome in the
245 cytosol(Ruggiano, Foresti, & Carvalho, 2014). We noted that treatment with the
246 proteasome inhibitor MG132 caused widespread accumulation of EMDΔ95-99 and EMD
247 throughout the NE/ER membrane network, cytoplasm, and nucleoplasm (Fig. 2E; 3B-C,
248 fourth panels) and accumulation of higher molecular weight forms of EMDΔ95-99 that
249 could be poly-ubiquitinated species (Fig. 3D). The widespread accumulation of EMD
250 throughout intracellular compartments upon proteasome inhibition suggests that newly
251 synthesized EMD variants are co-translationally degraded by the proteasome. Notably,
252 as a tail-anchored protein, EMD is post-translationally inserted into the ER membrane

253 and may be subject to quality control at this key step in biogenesis. Consistent with this,
254 we observe that non-membrane-associated and higher molecular weight forms of
255 EMDΔ95-99 accumulate upon proteasome inhibition (Fig. S3).

Figure 3. Effects of proteasomal inhibition and ERAD disruption on emerin protein levels.

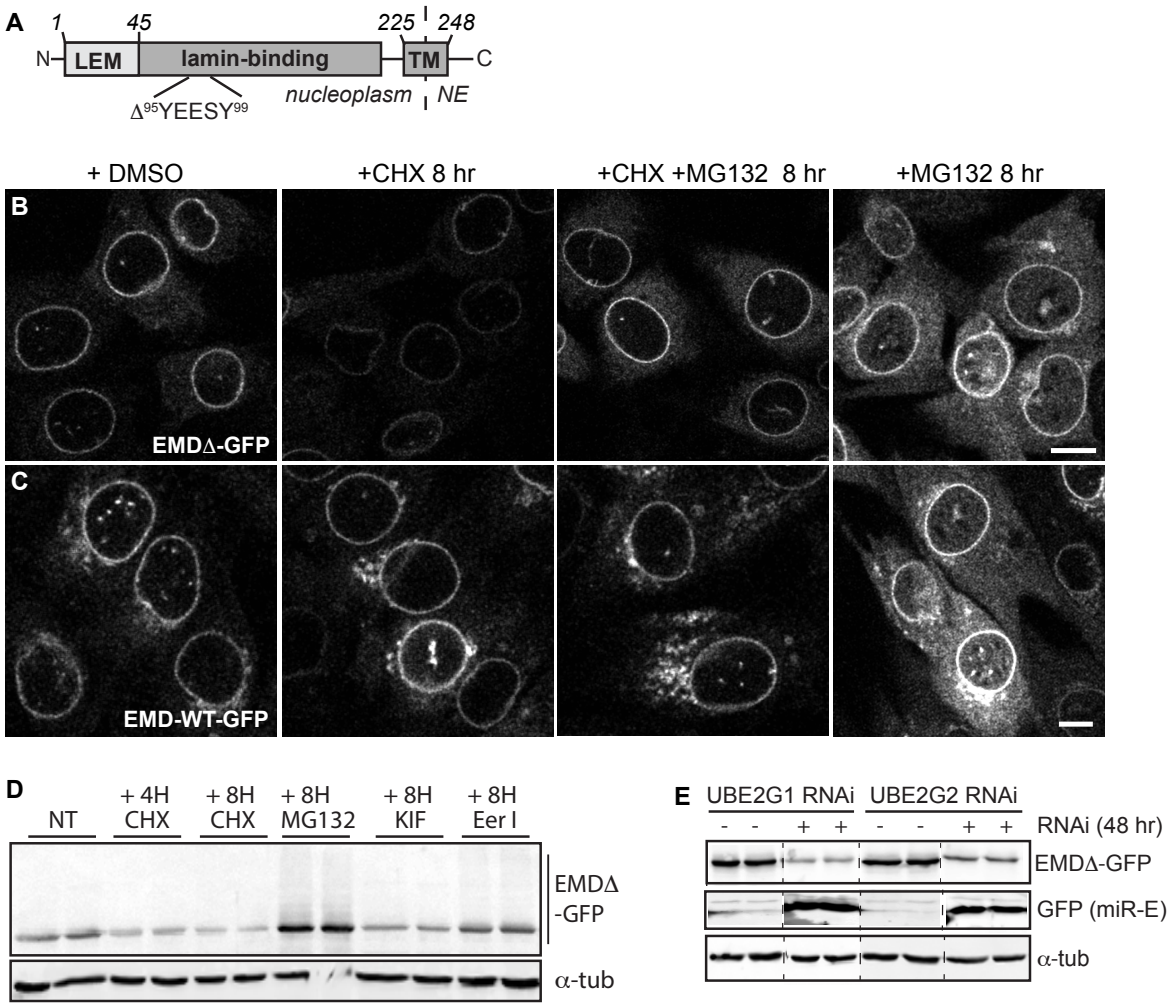

256

Figure 3. Effects of proteasomal inhibition and ERAD disruption on emerin protein levels. (A) Diagram of emerin domain organization and position of EDMD-linked in-frame deletion mutant (EMDΔ95-99) within the lamin-binding domain. (B-C) Representative confocal slices of cells stably expressing EMDΔ-GFP (B) or EMD-WT-GFP (C) and treated with DMSO vehicle control, CHX alone, CHX and MG132, or MG132 alone for 8 hours; scale bar, 10 μm. All images were acquired using the same laser power and detector gain settings. (D) Western blot analysis of protein levels in C2C12 cells stably expressing EMDΔ-GFP and treated with DMSO vehicle, the translation inhibitor CHX, or the proteasome inhibitor MG132 for the time periods shown. α-tubulin shown as loading control. (E) Western blot analysis of C2C12 cells stably expressing EMDΔ-GFP and doxycycline-inducible RNAi targeting the E2 ubiquitin ligases UBE2G1 and UBE2G2 and treated with DMSO vehicle control (-) or with doxycycline (+) for 48 hours. Free GFP indicates RNAi induction.

257 Conversely, we observed that mature wild type EMD accumulates gradually at the INM
258 when the proteasome is inhibited (Fig. 2F, G), and that EMD variants are modestly
259 stabilized at the INM in cells co-treated with the translation inhibitor CHX and MG132
260 (Fig. 3B-C, third panels). This could indicate that INM-localized EMD variants are
261 cleared by ERAD, which terminates in targeting to the proteasome. Indeed,
262 pharmacological inhibition of the ERAD ATPase p97 with the drug eeyarestatin I(Wang,
263 Li, & Ye, 2008) causes modest stabilization of EMDΔ95-99 and accumulation of higher
264 molecular weight species (Fig. 3D). In contrast, the drug kifunensine, which prevents
265 ERAD targeting of misfolded glycosylated proteins(Fagioli & Sitia, 2001), has no effect
266 on EMD levels as would be expected given the lack of glycosylation sites within EMD's
267 small luminal domain (Fig. 3D).
268
269 If EMD variants are subject to ERAD, inhibition of earlier steps in the ERAD pathway
270 should similarly cause accumulation of EMD variants. Ubiquitin is conferred to ERAD
271 substrates by E3 ubiquitin ligases, which each exhibit preference for a small number of
272 substrates. A few E3 ubiquitin ligases have been implicated in ERAD of INM-localized
273 substrates in yeast, including Doa10 and Asi1(Khmelinskii, Blaszczak, Pantazopoulou,
274 Fischer, Omnus, Le Dez, Brossard, Gunnarsson, Barry, Meurer, Kirrmaier, Boone,
275 Huber, Rabut, Ljungdahl, & Knop, 2014b). MARCH6 is a mammalian ortholog of
276 Doa10(Zattas, Berk, Kreft, & Hochstrasser, 2016). Mammalian orthologs of Asi1 have
277 not been identified. Based on iterative sequence homology analysis through the
278 MetaPhORs database(Pryszcz, Huerta-Cepas, & Gabaldón, 2010) we identified two
279 possible Asi1 homologs: Rnf26 and CGRRF1. We depleted MARCH6, Rnf26, and
280 CGRRF1 with short interfering RNA (siRNA), but observed no effect on EMDΔ95-99
281 protein levels (Fig. S4A), indicating that these ligases do not catalyze EMD turnover, or
282 alternatively that multiple E3 ligases are redundant in this process. Importantly, the
283 broad group of ERAD-implicated E3 ligases rely on a handful of E2 ubiquitin conjugating
284 enzymes for ubiquitin transfer. These E2 ligases – four in mammals – thus represent a
285 key control point for ERAD(Christianson, Olzmann, Shaler, Sowa, Bennett, Richter,
286 Tyler, Greenblatt, Wade Harper, et al., 2011b; Leto et al., 2019). We targeted these four
287 E2 ubiquitin ligases by siRNA transfection (Fig. S3B-C) and a subset of these by

288 inducible RNAi using a potent micro RNA-based system (Fellmann et al., 2013) (Fig.
289 3E; Fig. S3D) and analyzed the effects on EMDΔ95-99 levels. To our surprise,
290 knockdown of UBE2G1, UBE2G2, UBE2J1, and UBE2J2 either did not stabilize or
291 instead decreased EMDΔ95-99 levels (Fig. S3, Fig 3E). This finding suggests that when
292 ERAD is perturbed, EMD variants can be cleared by an alternative pathway.

Figure 4. Rapid clearance of emerin variants from the NE and ER during folding stress

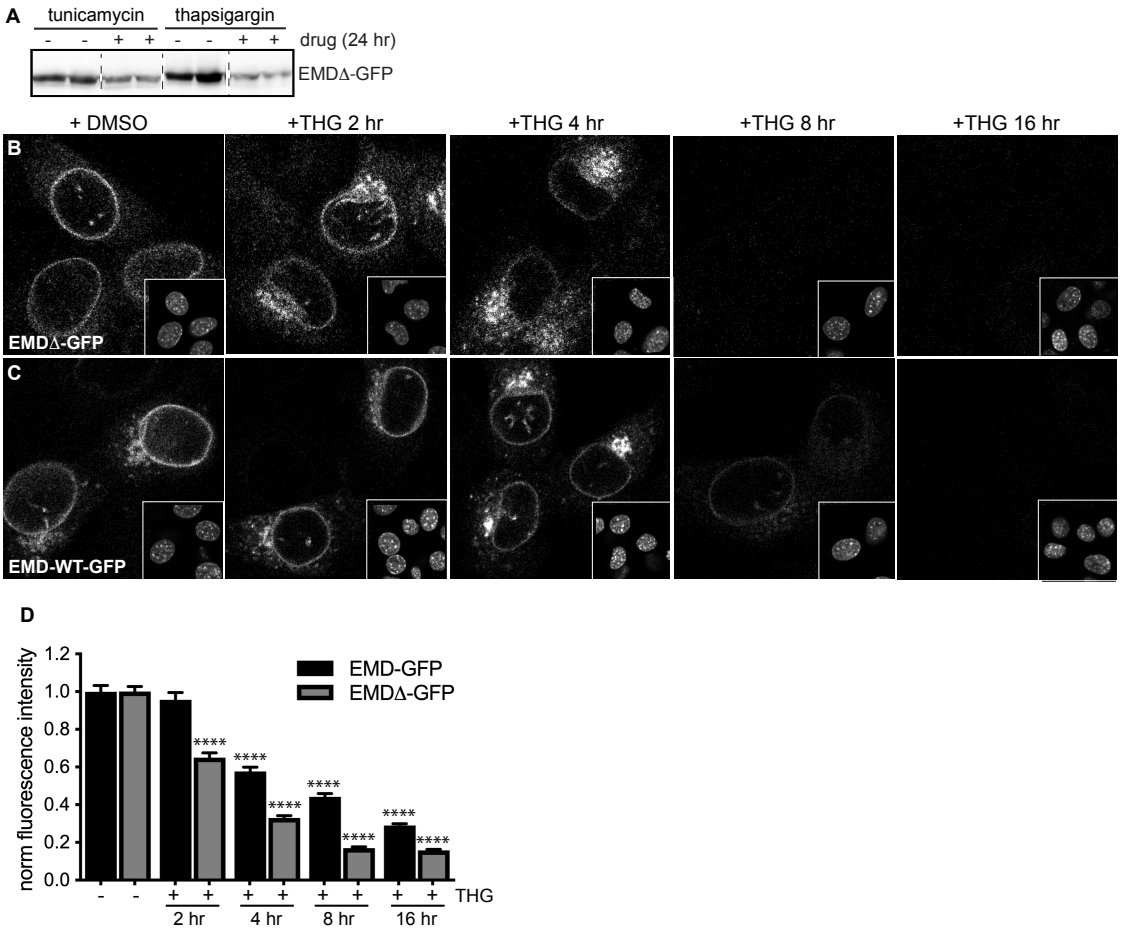

293

Figure 4. Rapid clearance of emerin variants from the NE and ER during folding stress. (A) Western blot analysis of C2C12 cells stably expressing EMDΔ-GFP and treated with DMSO vehicle control (-), tunicamycin (+), or thapsigargin (+) for 24 hours. (B-C) Timecourse of thapsigargin treatment and effects on GFP fusion protein levels. Representative confocal slices of C2C12 cells stably expressing EMDΔ-GFP (B) or EMD-WT-GFP (C) after treatment with DMSO vehicle control or with thapsigargin (THG) for the indicated time periods. Insets show nuclei in the same ~50 µm field of view stained with Hoechst. All images were acquired using the same laser power and detector gain settings. (D) Quantification of NE-localized GFP fluorescence intensity over THG treatment timecourse. Columns indicate average and error bars indicate SEM for N > 393 cells from 4 independent experiments. **** indicates p-value < 0.0001 compared to untreated (by t-test).

294

295 **Emerin is subject to rapid stress-dependent clearance from the ER and NE**
296 Global inhibition of ERAD places profound protein folding stress on the ER membrane
297 network and induces the unfolded protein response (UPR) (Christianson, Olzmann,
298 Shaler, Sowa, Bennett, Richter, Tyler, Greenblatt, Harper, et al., 2011a). We considered
299 whether direct induction of ER stress was sufficient to accelerate the turnover of
300 EMDΔ95-99. We tested the effects of the ER stressor tunicamycin, which interferes with
301 glycosylation and thus with protein folding, or the stressor thapsigargin, which disrupts
302 ER homeostasis by causing release of Ca2+ from the ER lumen, on EMDΔ95-99 protein
303 levels. Treatment with either thapsigargin or tunicamycin potently decreased EMDΔ95-
304 99 protein levels within 24 hours (Fig 4A).
305
306 We tracked EMDΔ95-99 protein localization by time-lapse microscopy in cells treated
307 with thapsigargin (Fig. 4B). Within 2 hours of treatment, NE localization of EMDΔ95-99
308 was significantly decreased, and its accumulation in a perinuclear membrane
309 compartment, likely the Golgi apparatus, became apparent. By 8 hours after
310 thapsigargin administration, EMDΔ95-99 was undetectable (Fig. 4B, D). We next asked
311 whether wild type EMD was also subject to this pathway; similarly to EMDΔ95-99, we
312 observed a time-dependent decrease of NE-localized protein, concomitant with
313 accumulation in a perinuclear compartment and followed by eventual disappearance of
314 the protein. Compared to EMDΔ95-99, displacement of wild type EMD from the NE
315 proceeded significantly more slowly (Fig. 4C-D). These data suggest that under
316 conditions of ER stress, EMD variants are cleared from the NE/ER membrane network
317 by transport out of the ER and eventual disposal of the protein in a post-ER
318 compartment.
319
320 **Stress-dependent clearance of emerin involves trafficking through the secretory**
321 **pathway**
322 Time-lapse imaging (Fig. 4B-C) suggested that in a rapid response to acute ER stress,
323 EMD variants traffic out of the NE/ER and concentrate in a perinuclear compartment.
324 Based on localization and morphology, we surmised that this compartment was the
325 Golgi apparatus. To test this, we evaluated the extent of colocalization of EMD variants

Figure 5. Emerin is trafficked out of the ER under ER stress

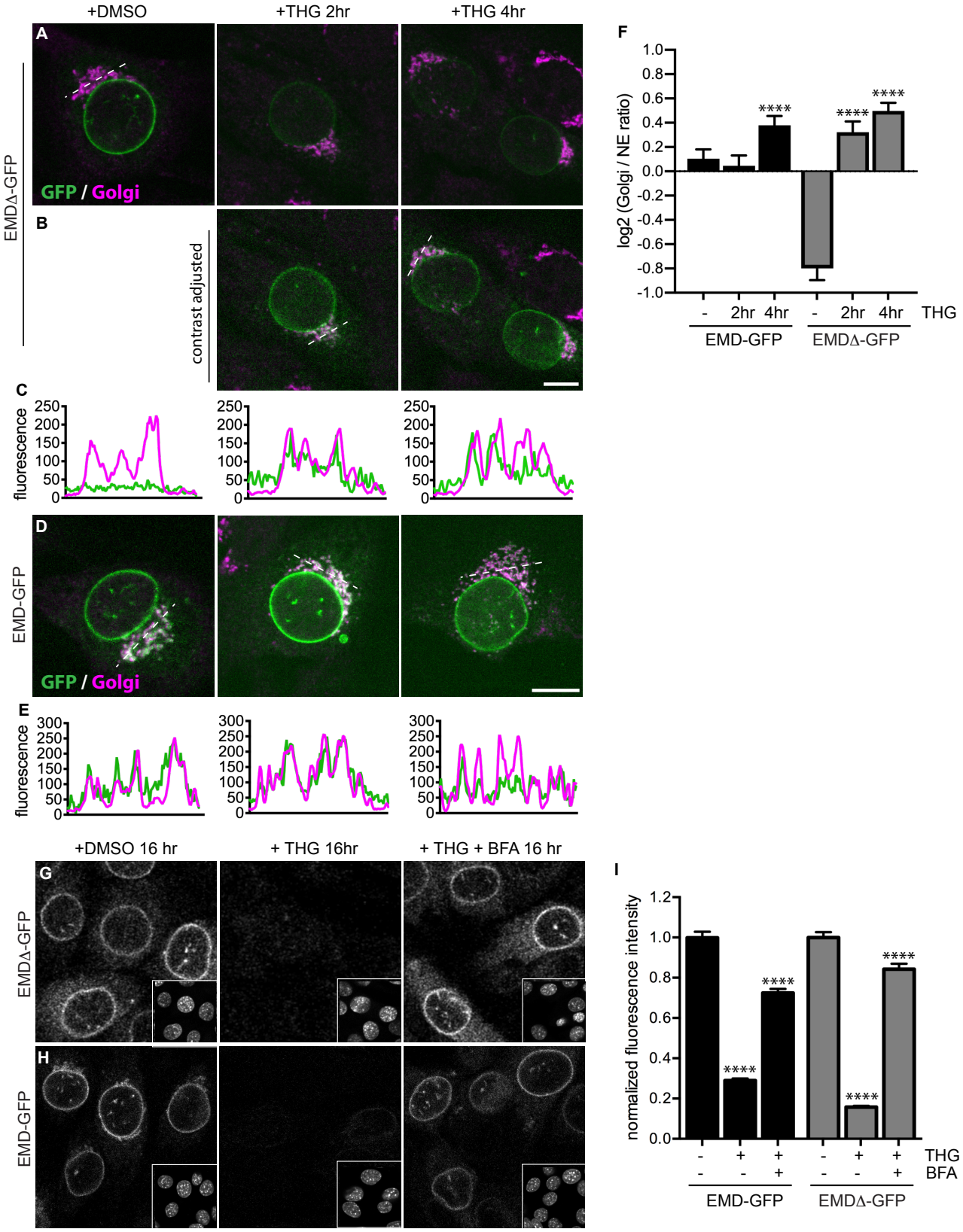

326

Figure 5. Emerin is trafficked out of the ER under ER stress. (A-B) Representative confocal slices of cells stably expressing EMDΔ-GFP, treated with DMSO or THG for the indicated times and costained for giantin to mark the Golgi. Dotted lines mark positions of linescans in (C). All images were acquired using the same laser power and detector gain settings, but selected images contrast-adjusted in bottom panel to show relative levels of EMDΔ-GFP in NE and Golgi. (D) Representative confocal slices of cells stably expressing EMD-GFP, treated with DMSO or THG for the indicated times and costained for giantin to mark the Golgi. Dotted lines mark positions of linescans in (E). (F) Quantification of GFP fluorescence intensity abundance ratio in Golgi *versus* NE over THG treatment timecourse. Columns indicate average with error bars indicating SEM for N > 37 cells from 2 independent experiments. **** indicates p-value < 0.0001 compared to untreated (by t-test). (G-H) Representative confocal slices of cells stably expressing EMDΔ-GFP (G) or EMD-WT-GFP (H) after 16 hours of treatment with DMSO vehicle control, THG, or co-treatment with THG and brefeldin A (BFA). Insets show nuclei in the same ~50 μm field of view stained with Hoechst. (I) Quantification of GFP fluorescence intensity at the NE across the conditions represented in (G-H). Columns indicate average with error bars indicating SEM for N > 386 cells from 3 independent experiments. **** indicates p-value < 0.0001 compared to untreated (by t-test).

with the medial Golgi resident protein giantin in untreated cells and cells that had been treated with THG for 2-4 hours (Fig. 5A-E). In untreated cells, EMDΔ95-99 did not enrich in the Golgi, but THG treatment rapidly induced Golgi colocalization as NE-localized EMDΔ95-99 levels decreased (Fig. 5A-C). Wild type EMD exhibited some occupancy in the Golgi under basal conditions that gradually increased upon ER stress (Fig. 5D-E). Comparing GFP fluorescence intensity in the Golgi *versus* the NE over time revealed that ER stress rapidly induces significant enrichment of EMDΔ95-99 in the Golgi over the NE within 2 hours, while wild type EMD becomes enriched in the Golgi with slower kinetics (Fig. 5F). This indicates that, during ER stress, EMD variants are cleared from the NE/ER by a pathway that involves transport to the Golgi, on a more rapid timescale for EMDΔ95-99 and on a slower timescale for wild type EMD.

Anterograde transport from the ER to the Golgi is mediated by packaging of cargoes within vesicles coated by the COPII vesicle formation machinery(Barlowe & Miller, 2013), a process which can be inhibited by the drug brefeldin A (BFA). To test whether EMD is a client of COPII-mediated ER-to-Golgi transport, we co-incubated cells expressing EMD or EMDΔ95-99 with thapsigargin and BFA. Strikingly, co-treatment with BFA reversed loss of EMD and EMDΔ95-99 from the NE (Fig 5G-H); under these conditions, protein levels were maintained to nearly the same extent as those observed

346 in untreated cells (Fig. 5I). Taken together with the time-dependent enrichment of EMD
347 variants in the Golgi apparatus (Fig. 5A-F), this indicates that under ER stress, EMD
348 variants can be cleared from both the NE and ER by vesicular transport through the
349 Golgi.
350
351 While vesicle-mediated transport is the major pathway by which proteins move from the
352 ER and onward through the secretory pathway, alternative modes of removing protein
353 from the ER exist, in particular during ER stress. Recent evidence indicates that the ER
354 can undergo autophagy under various conditions, including acute ER stress(Smith et
355 al., 2018). To evaluate the possibility that EMD variants could be engulfed and removed
356 from the NE and ER by autophagosomes, we tested the ability of the PI3K inhibitor
357 KU55933 to reverse EMD loss. PI3K signaling promotes the formation of isolation
358 membranes that engulf autophagic cargo, and KU55933 inhibits this(Farkas, Daugaard,
359 & Jäättelä, 2011; Klionsky et al., 2016). We observed that cotreatment with KU55933
360 during acute ER stress could not prevent loss EMD variants from the NE/ER (Fig. 6A-
361 C), in contrast to the ability of BFA treatment to rescue EMD loss. This indicates that
362 vesicle-mediated transport to the Golgi and not autophagic engulfment mediates EMD's
363 exit from the ER during stress.
364
365 Proteins in post-ER compartments can be degraded by vesicle-mediated traffic to the
366 lysosome(Saftig & Klumperman, 2009). To investigate whether the lysosome was the
367 eventual destination of EMD variants after ER export, we co-incubated cells expressing
368 EMD or EMDΔ95-99 with thapsigargin and bafilomycin A1 (Baf A1), which impairs
369 lysosome acidification and thus slows protein degradative processes within lysosomes.
370 Under these conditions, we observed complete translocation of both EMD and
371 EMDΔ95-99 out of the NE and ER and into perinuclear puncta that are likely lysosomes
372 based on their size, number, and location (Fig. 6E-F). This indicates that the eventual
373 destination of EMD variants after clearance from the stressed NE/ER network is the
374 lysosome.

Figure 6. Emerin trafficking is dependent on lysosomal but not autophagosomal function.

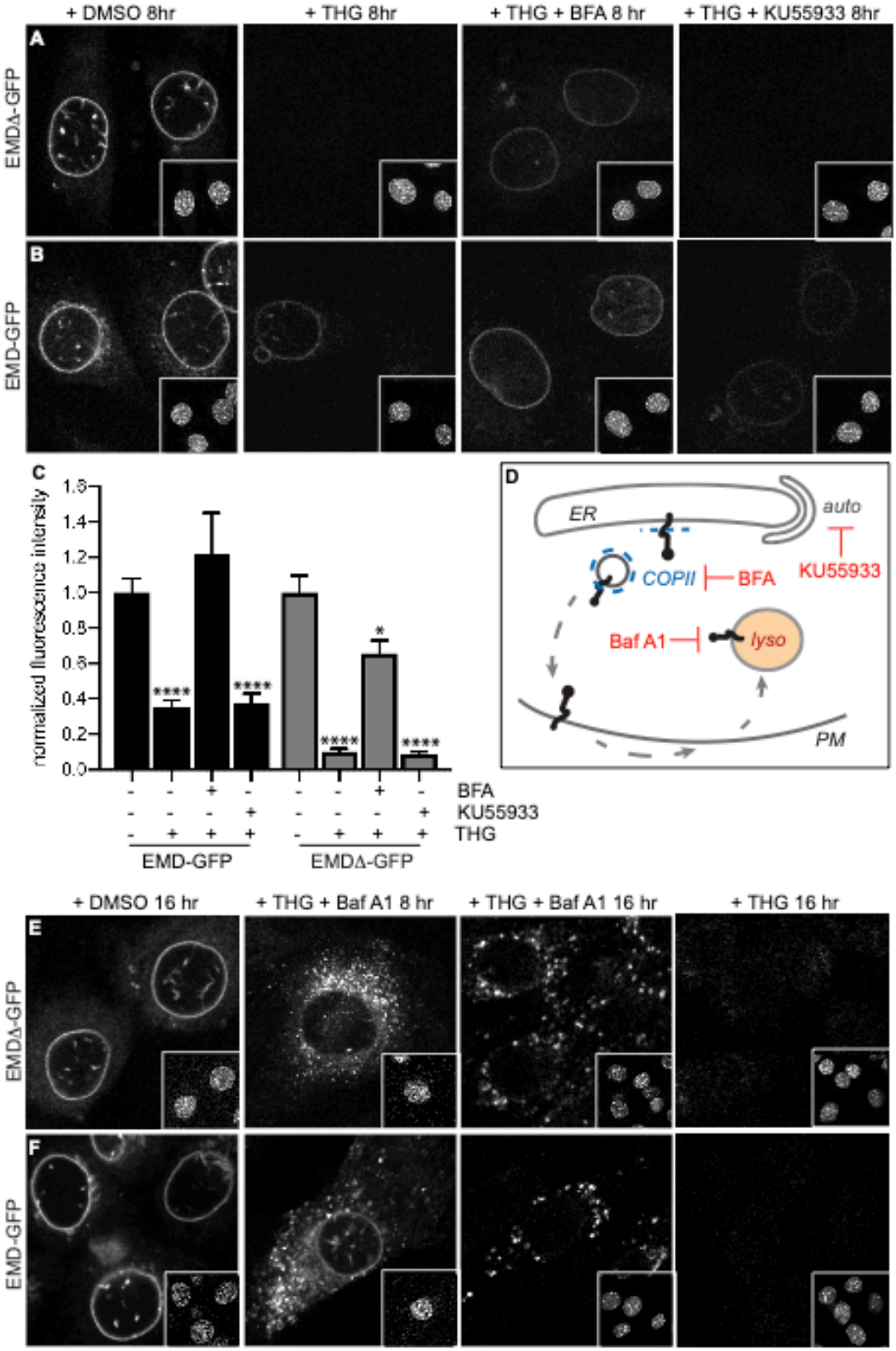

375

Figure 6. Emerin trafficking is dependent on lysosomal but not autophagosomal function. (A-B) Representative confocal slices of cells stably expressing EMD∆-GFP (A) or EMD-WT-GFP (B) after 8 hours of treatment with DMSO vehicle control, THG, co-treatment with THG and BFA, or co-treatment with THG and KU55933. Insets show nuclei in the same field of view stained with Hoechst. (C) Quantification of NE-localized GFP fluorescence intensity across the conditions shown in (A-B). Columns indicate average and error bars indicate SEM for N > 56 cells from 3 independent experiments. **** indicates p-value < 0.0001 compared to untreated (by t-test). (D) Diagram of processes perturbed by KU55933, BFA, and Baf A1 treatment. (E-F) Representative confocal slices of cells stably expressing EMD∆-GFP (E) or EMD-WT-GFP (F) after treatment with DMSO vehicle control, THG, or co-treatment with THG and Baf A1 for the indicated times. Insets show nuclei in the same ~50 µm field of view stained with Hoechst.

Emerin transiently accesses the plasma membrane during ER stress

A possible route from the early secretory pathway to the lysosome could involve anterograde transport following the "bulk flow" of the secretory pathway, through the Golgi and into vesicles destined for the plasma membrane (PM). There, mislocalized proteins may be selectively endocytosed and trafficked to lysosomes for degradation through retrograde transport(Saftig & Klumperman, 2009). To explore this possibility, we performed antibody uptake assays in cells expressing EMD or EMD∆95-99 under homeostatic or stressed conditions. EMD is a tail-anchored protein with its final C-terminal amino acids facing the ER lumen; when C-terminally tagged, the tag will face the extracellular space if EMD accesses the PM (Fig. 7A). We tested whether EMD's GFP tag is accessible to an anti-GFP antibody applied to the surface of intact cells. In untreated cells, low amounts of EMD∆95-99 (Fig. 7B-D) or EMD (Fig. 7E-G) are accessible to an anti-GFP antibody, but not to an anti-myc antibody, indicating that EMD variants are not completely restricted to intracellular membrane compartments under homeostatic conditions. Upon induction of ER stress by THG, the amount of PM-accessible EMD variants rapidly increases within 2-4 hours, and begins to taper off within 6 hours. This implies that ER stress induces the export of EMD variants from the NE/ER to the PM. Importantly, the GFP antibody signal is visible within intracellular puncta, consistent with EMD-GFP:antibody conjugates being rapidly internalized into vesicles after PM delivery. Based on the timescale when the levels of GFP-tagged EMD variants begin to significantly decrease at the NE (Fig. 4B-D), increase in the Golgi (Fig. 5A-F), transit through the PM (Fig. 7) and accumulate in lysosomes (Fig. 6E-F), we infer

400 that EMD variants are transported through the secretory pathway to the PM, then
401 internalized and delivered to lysosomes for degradation.

Figure 7. Emerin traffics through the plasma membrane upon ER stress

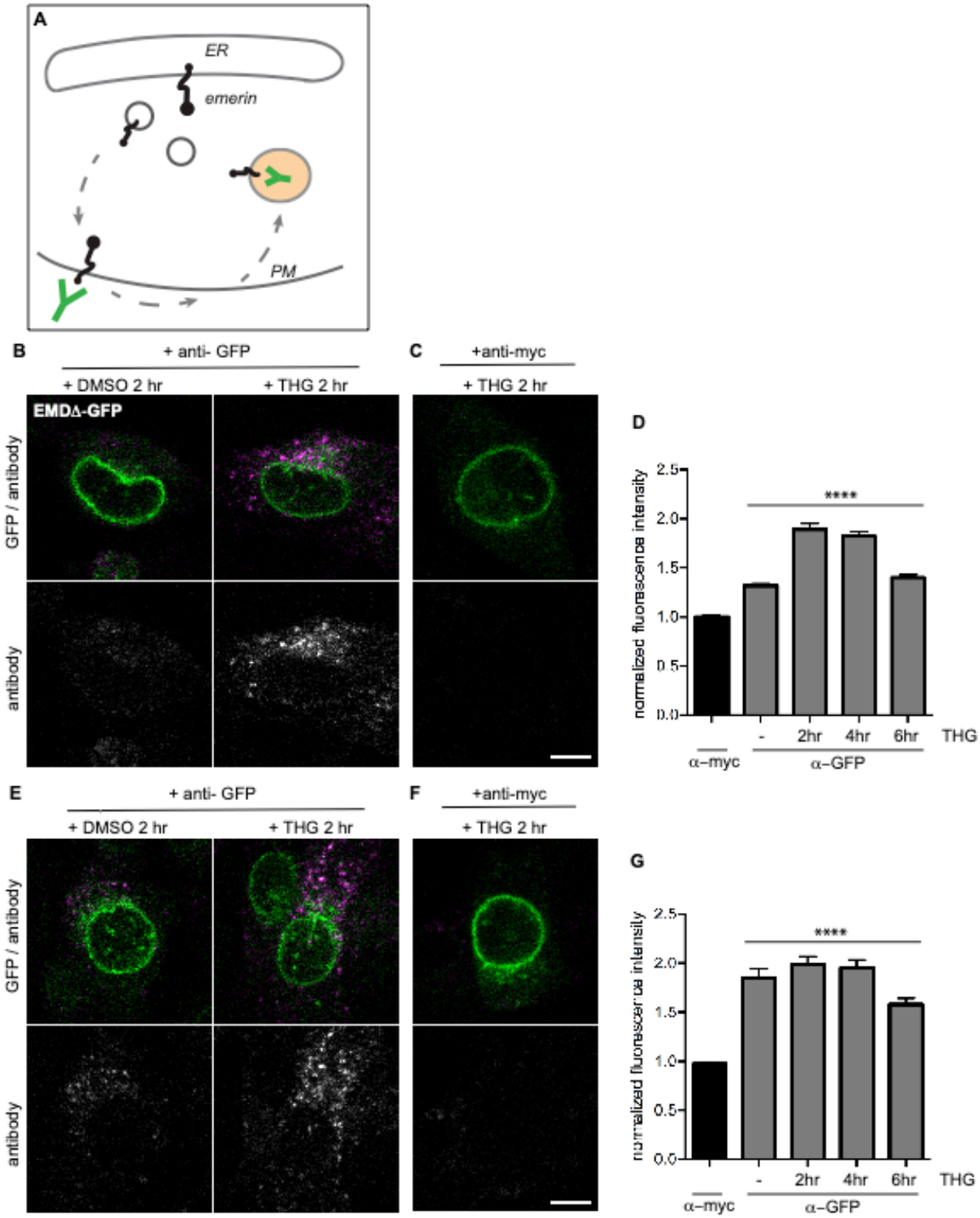

402

Figure 7. Emerin traffics through the plasma membrane upon ER stress. (A) Schematic of antibody uptake assay experimental design. If emerin accesses the plasma membrane (PM), it will be detected by anti-GFP antibody (green), which will bind the surface-exposed GFP tag. (B) Uptake of anti-GFP antibody or (C) anti-myc control antibody by cells stably expressing EMDΔ-GFP and treated with DMSO vehicle control or THG for 2 hours. (D) Quantification of internalized antibody signal in EMDΔ-GFP expressing cells. Columns indicate average and error bars indicate SEM for N > 235 cells from 3 independent experiments. **** indicates p-value < 0.0001 (t-test) compared to untreated. (E) Uptake of anti-GFP antibody or (F) anti-myc control antibody by cells stably expressing EMD-WT-GFP and treated with DMSO vehicle control or THG for 2 hours. (G) Quantification of internalized antibody signal in EMD-WT-GFP expressing cells. Columns indicate average and error bars indicate SEM for N > 66 cells from 2 independent experiments. **** indicates p-value < 0.0001 (t-test) compared to untreated. All images were acquired using the same laser power and detector gain settings. Scale bar, 10 μm.

Other INM proteins do not undergo stress-dependent clearance

Our findings indicate that EMD is subject to proteasome-dependent turnover at the INM (Fig. 2F, G; Fig. 3B-D), but can also be rapidly removed from the INM and ER membrane network and targeted for degradation during ER stress. This raises the possibility that additional INM proteins are susceptible to stress-dependent degradation. To address this, we tested the response of additional INM proteins to ER stress induction by THG, to ER export blockage by BFA, and to lysosomal maturation blockage by Baf A1. We selected proteins with distinct topologies and half-lives, including the long-lived polytopic INM protein nurim and the less stable single-pass transmembrane protein Sun2 (see Fig. 1H, Table S5). Prolonged treatment with THG modestly decreased nurim protein levels and significantly decreased Sun2 protein levels (Fig. 8A-C), likely as a consequence of translational inhibition caused by ER stress(Harding, Zhang, & Ron, 1999). Consistent with this interpretation, the sensitivity of these two proteins tracks with the relative differences in their half-lives (Table S5); nurim has a half-life of ~9 days, while Sun2 has a half-life of ~3 days in non-dividing cells. Importantly, however, co-incubation with THG and BFA had no effect on either the subcellular localization or abundance of nurim or Sun2 (Fig. 8A-C), indicating that they are not subject to stress-dependent ER export and degradation. Further, neither protein leaves the NE/ER to accumulate in lysosomes when lysosome acidification is blocked by Baf A1 (Fig. 8D, E). This indicates that stress-dependent trafficking out of the INM is selective, and that intrinsic features of EMD control its clearance from the NE/ER and

426 targeting into lysosomes.

Figure 8. Other INM proteins do not undergo stress-dependent clearance from the NE or access lysosomes.

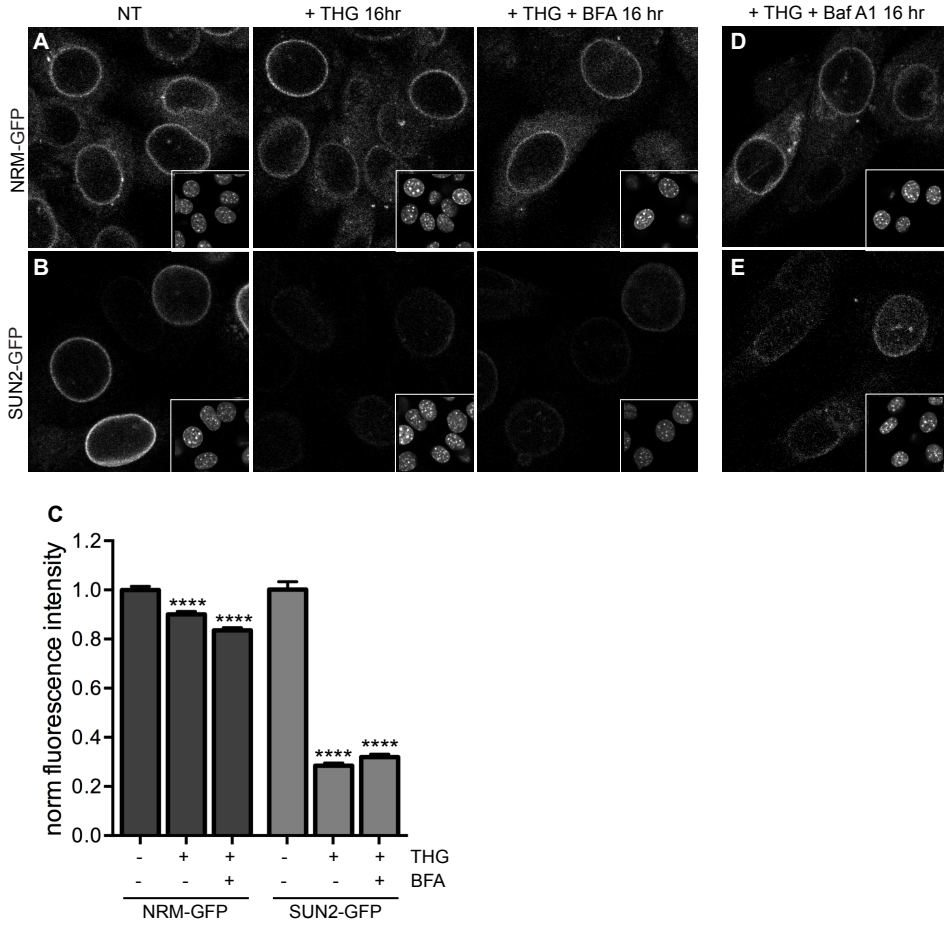

427

428

Figure 8. Other INM proteins do not undergo stress-dependent clearance from the NE and ER or access lysosomes. (A-B) Representative confocal slices of cells stably expressing NRM-GFP (A) or Sun2-GFP (B) after 16 hours of treatment with DMSO vehicle control, THG, or co-treatment with THG and BFA. Insets show nuclei in the same ~50 µm field of view stained with Hoechst. (C) Quantification of GFP fluorescence intensity at the NE across selected conditions represented in (A-B). Columns indicate average and error bars indicate SEM for N > 690 cells from 3 independent experiments. **** indicates p-value < 0.0001 compared to untreated (t-test). (D-E) Representative confocal slices of cells stably expressing NRM-GFP (D) or Sun2-GFP (E) after 16 hours of co-treatment with THG and BAF A1. All images were acquired using the same laser power and detector gain settings.

429

430 **A signal within emerin's LEM domain is required for stress-dependent export**

431 Why is EMD selectively targeted for stress-dependent clearance from the INM and ER?

432 We considered functional domains that might be involved in responding to ER stress.

433 EMD is a tail-anchored protein with a ~10 amino acid tail that protrudes into the ER
434 lumen (Fig. 3A). This short sequence lacks any glycosylation sites or other clear motifs
435 for engaging with proteins within the ER lumen. EMD's nucleoplasmic domain includes
436 an N-terminal LEM domain and an internal lamin A-binding region (Fig. 3A). Emerin
437 relies on lamin A for targeting to the INM(Vaughan et al., 2001) but we noted that in
438 *lmna* -/- MEFs, EMD-GFP remained stably expressed even while mislocalized to the
439 peripheral ER (Fig. S5). This indicates that dissociation from the lamina is not sufficient
440 to promote clearance of EMD from the NE/ER membrane system.
441 We next evaluated whether interactions mediated by the LEM domain could contribute
442 to stress-dependent EMD export. The LEM domain (Fig. 3A) is a protein fold that binds
443 with high affinity to the soluble nucleoplasmic protein BAF. We deleted this domain and
444 queried the effects on EMD localization and trafficking. When expressed within
445 unperturbed cells, EMDΔLEM exhibited normal enrichment in the NE (Fig. 9A),
446 consistent with its ability to bind the lamina via remaining intact protein domains.
447 However, we observed that this mutant was less responsive than wild-type EMD to ER
448 stress induction; NE-localized EMDΔLEM was clearly detectable over several hours of
449 THG treatment (Fig. 9A-C) and was significantly less sensitive than full-length EMD to
450 ER stress (Fig. 9C). We surmise that the eventual loss of EMDΔLEM is due to
451 translational inhibition resulting from ER stress(Harding et al., 1999). Consistent with the
452 interpretation that the LEM domain mediates post-ER trafficking, co-incubation of
453 EMDΔLEM-expressing cells with THG and BFA or Baf A1 each had no effect on protein
454 levels or localization (Fig. 9D-E). Altogether, this indicates that a signal within emerin's
455 LEM domain actively contributes to its selective export from the ER under stress
456 conditions.
457
458

Figure 9. A signal within emerin's LEM domain is required for RESET

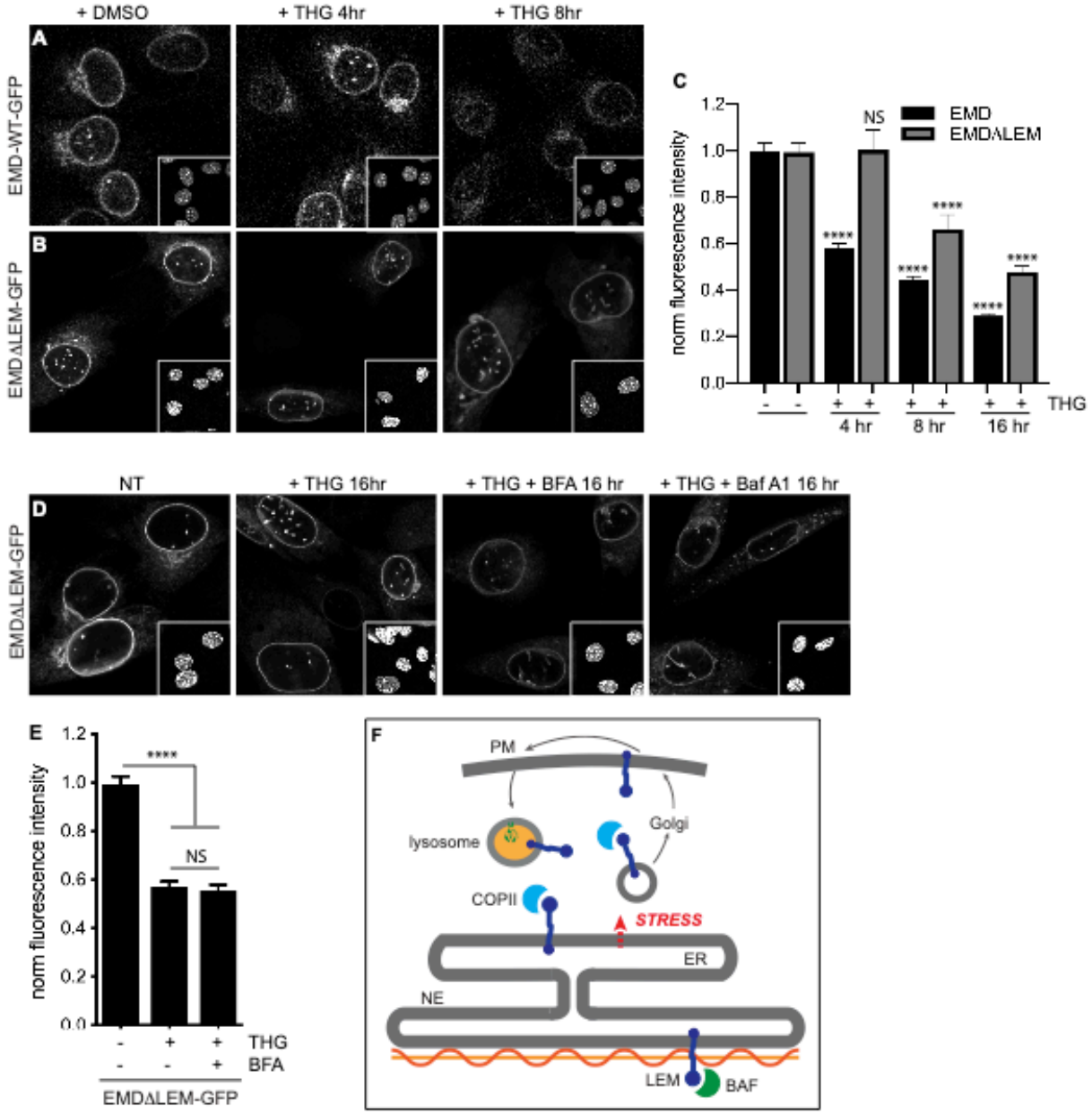

466

Figure 9. A signal within emerin's LEM domain is required for stress-dependent ER export. (A-B) Representative confocal slices of C2C12 cells stably expressing EMD-WT-GFP (A) or EMD∆LEM-GFP (B) after treatment with DMSO vehicle control, or THG for the indicated times. Insets show nuclei in the same ~50 µm field of view stained with Hoechst. (C) Quantification of GFP fluorescence intensity at the NE across the timecourse shown in (A-B). Columns indicate average and error bars indicate SEM for N > 146 cells from 3 independent experiments. **** indicates p-value < 0.0001 compared to untreated (t-test). (D) Representative confocal slices of C2C12 cells stably expressing EMD∆LEM-GFP after treatment with DMSO vehicle control, THG, THG + BFA, or THG + Baf A1. (E) Quantification of GFP fluorescence intensity at the NE across the conditions shown in (D). Columns indicate average and error bars indicate SEM for N > 776 cells from 3 independent experiments. **** indicates p-value < 0.0001 compared to untreated (t-test). (F) Competition model for emerin sorting via its LEM domain competitively binding to BAF or to the ER export machinery.

467

468

469 **Discussion**

470 In this work, we applied a dynamic proteomic strategy to define organelle-wide trends in
471 protein turnover across the NE/ER membrane network in mammalian cells. While the
472 INM is separated from the bulk ER by the selective barrier of the NPC, we observe no
473 difference in global protein turnover rates between the ER and INM compartments or
474 any correlation between INM protein size and turnover kinetics. This, along with specific
475 visualization of mature INM proteins by RITE tagging and microscopy (Fig. 2) and
476 previous studies(Tsai et al., 2016), suggests that turnover of INM proteins can be
477 effectively achieved *in situ*.

478

479 Moving forward with the rapidly turned over INM protein EMD as a model substrate for
480 dissecting INM protein turnover, we noted that turnover of maturely folded EMD exhibits
481 proteasome dependence at the INM (Fig. 2F), while nascent EMD rapidly accumulates
482 throughout multiple cellular compartments when the proteasome is inhibited (Fig. 2E;
483 Fig. 3B-C, fourth panels). Taken together, these observations lead us to infer that
484 mature EMD and potentially other INM proteins can be turned over *in situ* at the INM by
485 a pathway that terminates in proteasomal degradation, while immature EMD (and
486 potentially other INM proteins) is also subject to co-translational quality control that
487 terminates in proteasomal degradation. As proteasomal inhibition and p97 inhibition
488 each stabilize EMD (Fig. 3D), we propose that EMD is an ERAD client under some
489 conditions.

490

491 Surprisingly, however, we also find that the INM protein EMD can be selectively shunted
492 to an alternative turnover pathway under conditions of acute ER stress. This pathway is
493 rapidly induced by ERAD blockage or by pharmacological induction of acute ER protein
494 folding stress (Fig. 3E, Fig. 4) and requires COPII-mediated export out of the ER (Fig.
495 5). Notably, changes to EMD localization and levels are apparent within 2-4 hours of ER
496 stress induction, which is significantly earlier than the timescale required for full
497 activation of the unfolded protein response (UPR) by ER stress (Calfon et al., 2002).
498 Based on the transient appearance of EMD at the PM (Fig. 7) and its accumulation in
499 perinuclear puncta after lysosomal inhibition (Fig. 6), we infer that EMD transits through

500 the secretory pathway and is then internalized into lysosomes. This dynamic and
501 selective removal of an INM protein is quite surprising and is inconsistent with models of
502 the INM as a terminal depot for its resident proteins.
503
504 A recent description of the fate of a misfolded variant of the GPI-anchored prion protein,
505 PrP, during ER stress has some intriguing parallels to our findings(Satpute-Krishnan et
506 al., 2014). PrP is normally targeted to the PM, but a misfolded variant is retained within
507 the ER by persistent association with protein folding chaperones. Similarly to what we
508 observe for an INM protein, ER stress induces the rapid export of misfolded PrP through
509 the secretory pathway, followed by transit through the PM and internalization and
510 delivery to lysosomes for degradation. This mode of clearance was termed rapid ER
511 stress-induced export, or RESET(Satpute-Krishnan et al., 2014).
512
513 There are several notable contrasts between PrP's export from the peripheral ER and
514 EMD's export from the INM and ER. For instance, the topology of PrP and EMD are
515 quite distinct. As a GPI-anchored protein, misfolded PrP faces the lumen of the ER, and
516 an interaction between PrP and Tmp21, a sorting adapter for luminal proteins, controls
517 RESET(Satpute-Krishnan et al., 2014). In contrast, EMD is a tail-anchored protein, and
518 interactions mediated by EMD's nucleoplasmic-facing LEM domain (Fig. 9) control its
519 stress-dependent clearance.
520
521 PrP and EMD also exhibit distinct subcellular localization when not undergoing RESET.
522 Misfolded PrP is retained in the ER network until RESET is initiated, while EMD is
523 enriched in the INM and associated with the nuclear lamina (Fig. S2). Importantly, EMD
524 is small enough (~25 kDa) to diffuse freely across the NPC, meaning that it may release
525 INM-localized binding partners and sample the ER with some frequency. This spatial
526 separation between EMD's site of enrichment and its site of ER export may explain the
527 longer timescale of RESET for EMD (2-4 hours) compared to ER-localized misfolded
528 PrP (~1 hour) (Satpute-Krishnan et al., 2014).
529

530 Finally, PrP and EMD variants exhibit clear differences in selectivity for the RESET
531 pathway. Only misfolded, ER-retained mutants of PrP are subject to RESET. On the
532 other hand, both wild type EMD and a less stable disease-linked variant (EMDΔ95-99)
533 are subject to stress-dependent clearance, although EMDΔ95-99 is more rapidly
534 cleared from the NE and ER. Both EMD variants appear functional until ER stress is
535 induced, as judged by their localization and affinity for the INM (Fig. 3, Fig. S2). This
536 suggests that clearance of EMD from the NE/ER is not strictly contingent on protein
537 misfolding.
538
539 We find that selective, stress dependent clearance of EMD depends on its 45-amino
540 acid LEM domain. LEM domains bind dynamically to the small soluble protein BAF,
541 which exists in both nuclear and cytoplasmic pools(Shimi et al., 2004). One model that
542 could explain the dichotomy between LEM-mediated BAF binding and LEM-mediated
543 ER export is that BAF and an ER export-promoting factor bind competitively to the same
544 surface of EMD's LEM domain (Fig. 9F). It could be that acute ER stress is relayed to
545 EMD via a structural reorganization or post-translational modification that disrupts the
546 LEM:BAF interface. It is possible that this system could be used to rapidly remove EMD
547 in response to ER stress and potentially other physiological stressors. This could in turn
548 rapidly inhibit the normal functions of EMD at the INM, including participating in
549 mechanosensitive signaling pathways(Guilluy et al., 2014) and contributing to the
550 scaffolding of heterochromatic domains at the nuclear periphery(Demmerle, Koch, &
551 Holaska, 2013). Overall, our findings indicate that the INM can be rapidly remodeled in
552 response to environmental stimuli, and that the function of the INM protein EMD may be
553 dynamically controlled by integration of environmental inputs via its LEM domain.
554
555 Notably, muscular dystrophy and cardiomyopathy diseases are caused by loss-of-
556 function mutations to EMD, many of which further destabilize the protein(Bonne &
557 Quijano-Roy, 2013; Fairley et al., 1999). We find evidence that a muscular dystrophy-
558 linked EMD variant (EMDΔ95-99) is more rapidly degraded under acute stress
559 conditions, suggesting that over-sensitization to ER stress could contribute to EMD-
560 linked diseases. EMD is broadly expressed(Uhlen et al., 2015), but mutations

561 predominantly affect muscle tissues. Intriguingly, skeletal muscle undergoes significant
562 ER stress both during development and during normal function(Deldicque, Hespel, &
563 Francaux, 2012). We speculate that these features of muscle physiology may make
564 muscle-localized EMD mutants especially vulnerable to ER stress-induced degradation.
565
566 **Materials and Methods**
567
568 **SILAC labeling**
569
570 SILAC labeling was performed as a pulse-chase(Ong & Mann, 2007). Proliferating
571 C2C12 mouse myoblasts were subcultured for >5 population doublings in culture
572 medium containing stable heavy isotopes of lysine and arginine ($^{13}C_6$-Lysine, $^{13}C_6$, $^{15}N_4$-
573 Arginine) to completely label the cellular proteome. Cells were grown in SILAC-
574 formulated DMEM lacking lysine and arginine and supplemented with 20% dialyzed
575 FBS, penicillin/streptomycin, and SILAC amino acids. Complete label incorporation was
576 verified by LC-MS/MS. Myoblasts were then grown to confluency and switched to
577 differentiation medium containing heavy isotopes for 5 days to induce myotube
578 differentiation. Differentiation medium contained SILAC DMEM, 2% dialyzed FBS,
579 penicillin/streptomycin, and SILAC amino acids. Media was refreshed every other day.
580 After differentiation, the mature myotube culture was switched to low serum
581 differentiation medium containing the normal isotopes of lysine and arginine: $^{12}C_6$-
582 Lysine, $^{12}C_6$, $^{14}N_4$-Arginine for 1-3 days.
583 Crude nuclear extracts were prepared similarly to previous work(Buchwalter & Hetzer,
584 2017; Schirmer et al., 2003). Cells were harvested by scraping into PBS, then swollen in
585 hypotonic lysis buffer (10 mM potassium acetate, 20 mM Tris acetate pH 7.5, 0.5 mM
586 DTT, 1.5 mM MgCl2, and protease inhibitors), followed by mechanical lysis through a
587 25-gauge needle and syringe. The nuclei were pelleted and the supernatant (containing
588 cytosol) was decanted. Nuclei were then resuspended in buffer containing 10 mM Tris
589 pH 8.0, 10% sucrose, 1 mM DTT, 0.1 mM MgCl2, 20 ug/ml DNase I, and 1 ug/ml
590 RNase I. After nuclease treatment, nuclei were layered on top of a 30% sucrose
591 cushion and pelleted. Crude nuclei were then extracted in 10 mM Tris pH 8, 1% n-octyl

592 glucoside, 400 mM NaCl, and 1 mM DTT, and extracts and pellets were prepared
593 separately for liquid chromatography-mass spectrometry.
594
595 **LC-MS/MS**
596 Samples were denatured in 8M urea/100 mM TEAB, pH 8.5; reduced with TCEP;
597 alkylated with chloroacetamide; and digested overnight with trypsin. Digestion was
598 quenched with 5% formic acid. Detergent was removed from pulse-labeled SILAC
599 samples with SCX tips (EMD Millipore). Samples were run on a Thermo Orbitrap Fusion
600 Tribrid MS/MS with CID fragmentation. The digest was injected directly onto a 30 cm,
601 75 um ID column packed with BEH 1.7 um C18 resin. Samples were separated at a flow
602 rate of 200 nl/min on a nLC 1000. Buffer A and B were 0.1% formic acid in water and
603 acetonitrile, respectively. A gradient of 1-25% B over 160 min, an increase to 35% B
604 over 60 min, an increase to 90% B over another 10 min and a hold at 90%B for a final
605 10 min of washing was used for a total run time of 240 min. The column was re-
606 equilibrated with 20 ul of buffer A prior to the injection of sample. Peptides were eluted
607 directly from the tip of the column and nanosprayed into the mass spectrometer by
608 application of 2.5 kV voltage at the back of the column. The Orbitrap Fusion was
609 operated in data dependent mode. Full MS1 scans were collected in the Orbitrap at
610 120K resolution with a mass range of 400 to 1500 m/z and an AGC target of 4e. The
611 cycle time was set to 3 s, and within this 3 s the most abundant ions per scan were
612 selected for CID MS/MS in the ion trap with an AGC target of 1e and minimum intensity
613 of 5000. Maximum fill times were set to 50 ms and 100 ms for MS and MS/MS scans,
614 respectively. Quadrupole isolation at 1.6 m/z was used, monoisotopic precursor
615 selection was enabled, charge states of 2-7 were selected and dynamic exclusion was
616 used with an exclusion duration of 5 s.
617
618 **Analysis of proteomic data**
619
620 Peptide and protein identification, quantification, and analysis were performed with
621 Integrated Proteomics Pipeline (IP2) (Integrated Proteomics Applications;
622 www.integratedproteomics.com). Tandem mass spectra were extracted from raw files

using RawConverter(He, Diedrich, Chu, & Yates, 2015) and searched with ProLUCID(Xu et al., 2015) against the mouse UniProt database (ID). The search space included all fully tryptic and half-tryptic peptide candidates. Carbamidomethylation on cysteine was allowed as a static modification. Data were searched with 50 ppm precursor ion tolerance and 600 ppm fragment ion tolerance. Data were filtered to 10 ppm precursor ion tolerance post-search. Identified proteins were filtered using DTASelect(Tabb, McDonald, & Yates, 2002) and utilizing a target-decoy database strategy to control the false discovery rate to 1% at the protein level. Census2(Park et al., 2014) was used for quantitative analysis of SILAC-labeled peptides. Peptides were subjected to stringent quality control criteria before inclusion in half-life determination analyses. Firstly, any peptide with a profile score < 0.8 was discarded. Secondly, peptides were filtered based on the extent of correlation between the heavy and light chromatograms, which is quantified as a regression score in Census. Peptides with extreme area ratios (less than 0.111 or greater than 9) were retained only if their regression score was > 0. Peptides with intermediate area ratios (between 0.111 and 9) were retained only if their regression score was > 0.8.

Half-life calculation

For estimation of protein half-lives, we restricted our analysis to peptides that were detected in at least 3 timepoints. 1685 proteins passed this criterion with at least 1 peptide; individual peptides and protein-level data are reported in Tables S1 and S2, respectively. Area ratio values were transformed into % old values using the following equation:

$$\%old = 100 * (1/(1+ AR))$$

And individual peptides were fit to a line corresponding to the following equation:

$$Ln(\%old) = kt + a$$

653 Individual peptide fits with $r^2 > 0.8$ and values of $k < 0$ were retained for protein-level
654 estimation of half-life. The slope of the fit for all peptides detected were averaged to
655 produce an average value and standard deviation at the protein level. These average
656 slope values were converted to half-life estimates using the equation below.
657
658 $T1/2 = - \ln(2)/k$
659
660 These values are reported in Table S3 for 1677 proteins. While calculated half-lives
661 range from ~0.33 days to ~30 days, we note that half-lives at either extreme should be
662 considered rough estimates of protein stability. For illustration, we have included
663 example fits for proteins in Figure S1 with predicted half-lives of 0.5 day, 1 day, 2 days,
664 4 days, 8 days, and 16 days. Linear regression predicts half-life well under conditions
665 where a line can be fit with high fidelity and a non-zero slope is detectable. We note the
666 good performance and clear distinctions in slope for proteins with predicted half-lives
667 ranging from 1 to 8 days, and observed more frequent deviations in linearity at the low
668 extreme (predicted T1/2 <1 day) and slopes approaching zero at the high extreme
669 (predicted T1/2 > 8 days). We expect that these factors limit the precision of half-life
670 determination below 1 day and above 8 days from a 3-day timecourse. Shorter or longer
671 timecourses would be required to investigate turnover at these timescales.
672
673 The TMHMM server(Krogh, Larsson, Heijne, & Sonnhammer, 2001) was used to define
674 the positions of transmembrane domains in INM proteins and infer extraluminal domain
675 sequences.
676
677 **Plasmid construction and cell line generation**
678 All emerin constructs are based on the emerin sequence from mouse (Uniprot ID
679 O08579); all nurim constructs based on the nurim sequence from mouse (Uniprot ID
680 Q8VC65); and all Sun2 constructs based on the Sun2 sequence from mouse (Uniprot
681 ID Q8BJS4). Emerin, Sun2, and nurim were each C-terminally tagged with GFP by
682 stitching PCR(Heckman & Pease, 2007), where each open reading frame was amplified
683 with the start codon included and the stop codon omitted, while GFP was amplified with

684 its start codon omitted and stop codon included. Primersets were designed with
685 overhangs including homology between each ORF and GFP, so that a second round of
686 PCR with flanking primers and the first two PCR products used as templates generates
687 an ORF-GFP fusion. EMDΔ95-99 was generated by Quickchange mutagenesis of the
688 emerin-GFP sequence followed by sequence verification. EMDΔLEM-GFP was
689 constructed by stitching PCR of emerin nucleic acid sequence 136-777 corresponding
690 to residues 46-258 of emerin protein with the stop codon omitted. A new ATG start
691 codon was introduced by PCR, and the C-terminal GFP tag introduced by stitching
692 PCR. All ORFs were introduced into the pQCXIB vector(Campeau et al., 2009) for
693 retroviral delivery and constitutive expression under a CMV promoter by Gateway
694 cloning.
695
696 INM-RITE tag plasmids were constructed as described in(Toyama et al., 2019). ORFs
697 of interest were introduced into the FLAG/myc-RITE or myc/FLAG-RITE plasmid
698 backbones, then the entire ORF-RITE construct was amplified and recombined into a
699 pDONR207 Gateway entry vector, followed by recombination into the pQCXIB retroviral
700 vector for constitutive mammalian expression.
701
702 UBE2G1, UBE2G2, UBE2J1, and MARCH6 miR-E inducible RNAi plasmids were
703 constructed as described in(Fellmann et al., 2013). Validated shRNA sequences with
704 the highest score for targeting mouse UBE2G1, UBE2G2, UBE2J1, and MARCH6 were
705 selected from the shERWOOD database (www.sherwood.cshl.edu), and ~100 bp
706 oligonucleotides with the corresponding sequence were synthesized. This sequence
707 was amplified by PCR using degenerate primers with XhoI and EcoRI restriction sites.
708 The PCR was digested with XhoI and EcoRI, gel purified, and ligated into the
709 LT3GEPIR lentiviral vector for doxycycline-inducible RNAi expression with GFP reporter
710 fluorescence. The LT3GEPIR vector was the kind gift of Johannes Zuber.
711
712 miR-E oligonucleotide sequences:
713

714 UBE2G1:
715 TGCTGTTGACAGTGAGCGAAAGACAGCTGGCAGAACTCAATAGTGAAGCCACAGA
716 TGTATTGAGTTCTGCCAGCTGTCTTCTGCCTACTGCCTCGGA
717
718 UBE2G2:
719 TGCTGTTGACAGTGAGCGAACCGGGAGCAGTTCTATAAGATAGTGAAGCCACAGA
720 TGTATCTTATAGAACTGCTCCCGGTCTGCCTACTGCCTCGGA
721
722 UBE2J1:
723 TGCTGTTGACAGTGAGCGAAAGGTTGTCTACTTCACCAGATAGTGAAGCCACAGAT
724 GTATCTGGTGAAGTAGACAACCTTCTGCCTACTGCCTCGGA
725
726 MARCH6:
727 TGCTGTTGACAGTGAGCGACTGGATCTTCATTCTTATTTATAGTGAAGCCACAGAT
728 GTATAAATAAGAATGAAGATCCAGCTGCCTACTGCCTCGGA
729
730 **RITE tag switching**
731
732 RITE tag switching experiments were performed in quiescent C2C12 cells stably
733 expressing RITE-tagged INM proteins. C2C12s were grown in Ibidi chamber slides and
734 induced to enter quiescence as previously described(K. Zhang, Sha, & Harter, 2010) by
735 growing C2C12 myoblasts to ~75% confluence, washing twice in warm PBS, and
736 switching to quiescent medium (DMEM without methionine, 2% FBS, and pen-strep).
737 Cells were maintained in quiescent medium for 3 days with media changes every other
738 day before initiation of RITE timecourses. To induce tag exchange, concentrated
739 adenovirus expressing Cre recombinase was added to the culture medium. Tag
740 switching was initiated at the indicated timepoints such that the entire slide containing
741 all time points could be fixed, stained, imaged, and quantified in parallel. To quantify
742 loss of “old” RITE-tagged protein over time, intensity per unit area of the “old” tag was
743 quantified across all conditions. Background measurements were taken from cell-free

744 regions of the imaging dish and subtracted from all signals as a background correction.
745 All signals were then normalized to the day 0 timepoint (no tag switch).
746
747 **Antibody uptake assays**
748 For antibody uptake assays, cells were pre-treated with drugs for the indicated times,
749 then incubated in medium containing antibody, drug, and 125 μM leupeptin for 1 hour
750 before fixation in paraformaldehyde and staining. Cells were stained with Alexa Fluor-
751 conjugated secondary antibody to visualize internalized primary antibody:GFP
752 conjugates. Cell surfaces were stained with Alexa Fluor-conjugated WGA; the WGA
753 signal was used as a guide for outlining individual cells and quantifying internalized
754 antibody fluorescence.
755
756 **Preparation of protein lysates and Western blotting**
757 Cells were washed in PBS, then lysed directly in plates in PBS lysis buffer (PBS
758 supplemented with 1% Triton-X-100, 0.1% SDS, and protease inhibitors). Cells were
759 further lysed by passage through a 25-gauge needle. Protein concentrations were
760 quantified by BCA assay, and ~20 ug of total protein was loaded per lane of 4-12%
761 gradient gels (Invitrogen). Blots were incubated with emerin antibody (1:1000) or alpha-
762 tubulin antibody (1:5000) followed by IR Dye-conjugated secondary antibodies (1:5000)
763 for multiplexed detection on the Odyssey imaging system.
764
765 **Microscopy and image analysis**
766 Cells were grown in Ibidi culture chambers, treated as indicated, and fixed in 4% PFA
767 for 5 minutes, then permeabilized in IF buffer (PBS, 0.1% Tx100, 0.02% SDS, 10 mg/ml
768 BSA) before staining with Hoechst DNA dye. Wells were rinsed in PBS before imaging
769 on a Zeiss LSM 710 scanning confocal microscope with a 63 x 1.4 NA objective.
770 Images shown are single confocal slices. All image quantification was performed on
771 maximum intensity projections of z-series with ImageJ. To quantify NE-localized protein
772 levels, the DNA stain was used as a mask, and all GFP fluorescence within that mask
773 was quantified.
774

775 **Antibodies and reagents**

776 Myc antibody 9B11 (Cell Signaling)

777 FLAG antibody M2 monoclonal (Sigma-Aldrich)

778 GFP antibody polyclonal rabbit (ab290, Abcam)

779 Emerin antibody polyclonal rabbit (sc-15378, Santa Cruz Biotech)

780 Alexa 647-WGA (Life Tech)

781 Giantin antibody polyclonal rabbit (PRB-114C, BioLegend)

782

783 These drugs were used at the following concentrations: cycloheximide (200 ug/ml),
784 MG132 (10 uM) thapsigargin (0.1 uM), tunicamycin (2 ug/ml), brefeldin A (2.5 uM),
785 bafilomycin A1 (100 nM), KU55933 (2 uM).

786

787 **References**

788

789 Albert, S., Schaffer, M., Beck, F., Mosalaganti, S., Asano, S., Thomas, H. F., et al.
790 (2017). Proteasomes tether to two distinct sites at the nuclear pore complex.
791 *Proceedings of the National Academy of Sciences*, *114*(52), 13726–13731.
792 http://doi.org/10.1073/pnas.1716305114

793 Barlowe, C. K., & Miller, E. A. (2013). Secretory Protein Biogenesis and Traffic in the
794 Early Secretory Pathway. *Genetics*, *193*(2), 383–410.
795 http://doi.org/10.1534/genetics.112.142810

796 Boni, A., Politi, A. Z., Strnad, P., Xiang, W., Hossain, M. J., & Ellenberg, J. (2015). Live
797 imaging and modeling of inner nuclear membrane targeting reveals its molecular
798 requirements in mammalian cells. *The Journal of Cell Biology*, *209*(5), 705–720.
799 http://doi.org/10.1083/jcb.201409133

800 Bonne, G., & Quijano-Roy, S. (2013). Emery-Dreifuss muscular dystrophy,
801 laminopathies, and other nuclear envelopathies. *Pediatric Neurology, Part III* (1st
802 ed., Vol. 113, pp. 1367–1376). Elsevier B.V. http://doi.org/10.1016/B978-0-444-
803 59565-2.00007-1

804 Brachner, A., & Foisner, R. (2011). Evolvement of LEM proteins as chromatin tethers at
805 the nuclear periphery. *Biochemical Society Transactions*, *39*(6), 1735–1741.
806 http://doi.org/10.1042/BST20110724
807 Buchwalter, A., & Hetzer, M. W. (2017). Nucleolar expansion and elevated protein
808 translation in premature aging. *Nature Communications*, 1–13.
809 http://doi.org/10.1038/s41467-017-00322-z
810 Calfon, M., Zeng, H., Urano, F., Till, J. H., Hubbard, S. R., Harding, H. P., et al. (2002).
811 IRE1 couples endoplasmic reticulum load to secretory capacity by processing the
812 XBP-1 mRNA. *Nature*, *415*(6867), 92–96. http://doi.org/10.1038/415092a
813 Cambridge, S. B., Gnad, F., Nguyen, C., Bermejo, J. L., Krüger, M., & Mann, M. (2011).
814 Systems-wide Proteomic Analysis in Mammalian Cells Reveals Conserved,
815 Functional Protein Turnover. *Journal of Proteome Research*, *10*(12), 5275–5284.
816 http://doi.org/10.1021/pr101183k
817 Campeau, E., Ruhl, V. E., Rodier, F., Smith, C. L., Rahmberg, B. L., Fuss, J. O., et al.
818 (2009). A Versatile Viral System for Expression and Depletion of Proteins in
819 Mammalian Cells. *PLoS ONE*, *4*(8), e6529–18.
820 http://doi.org/10.1371/journal.pone.0006529
821 Christianson, J. C., Olzmann, J. A., Shaler, T. A., Sowa, M. E., Bennett, E. J., Richter,
822 C. M., Tyler, R. E., Greenblatt, E. J., Harper, J. W., et al. (2011a). Defining human
823 ERAD networks through an integrative mapping strategy. *Nature Publishing Group*,
824 *14*(1), 93–105. http://doi.org/10.1038/ncb2383
825 Christianson, J. C., Olzmann, J. A., Shaler, T. A., Sowa, M. E., Bennett, E. J., Richter,
826 C. M., Tyler, R. E., Greenblatt, E. J., Wade Harper, J., et al. (2011b). Defining
827 human ERAD networks through an integrative mapping strategy. *Nature Cell*
828 *Biology*, *14*(1), 93–105. http://doi.org/10.1038/ncb2383
829 D'Angelo, M. A., Raices, M., Panowski, S. H., & Hetzer, M. W. (2009). Age-Dependent
830 Deterioration of Nuclear Pore Complexes Causes a Loss of Nuclear Integrity in
831 Postmitotic Cells. *Cell*, *136*(2), 284–295. http://doi.org/10.1016/j.cell.2008.11.037
832 Deldicque, L., Hespel, P., & Francaux, M. (2012). Endoplasmic reticulum stress in
833 skeletal muscle: origin and metabolic consequences. *Exercise and Sport Sciences*
834 *Reviews*, *40*(1), 43–49. http://doi.org/10.1097/JES.0b013e3182355e8c

835 Demmerle, J., Koch, A. J., & Holaska, J. M. (2013). Emerin and histone deacetylase 3
836 (HDAC3) cooperatively regulate expression and nuclear positions of MyoD, Myf5,
837 and Pax7 genes during myogenesis. *Chromosome Research*, *21*(8), 765–779.
838 http://doi.org/10.1007/s10577-013-9381-9
839 Deshaies, R. J., & Joazeiro, C. A. P. (2009). RING Domain E3 Ubiquitin Ligases.
840 *Annual Review of Biochemistry*, *78*(1), 399–434.
841 http://doi.org/10.1146/annurev.biochem.78.101807.093809
842 Dörrbaum, A. R., Kochen, L., Langer, J. D., & Schuman, E. M. (2018). Local and global
843 influences on protein turnover in neurons and glia. *eLife*, *7*, 489.
844 http://doi.org/10.7554/eLife.34202
845 Fagioli, C., & Sitia, R. (2001). Glycoprotein Quality Control in the Endoplasmic
846 Reticulum. *Journal of Biological Chemistry*, *276*(16), 12885–12892.
847 http://doi.org/10.1074/jbc.M009603200
848 Fairley, E. A., Kendrick-Jones, J., & Ellis, J. A. (1999). The Emery-Dreifuss muscular
849 dystrophy phenotype arises from aberrant targeting and binding of emerin at the
850 inner nuclear membrane. *Journal of Cell Science*, *112 (Pt 15)*, 2571–2582.
851 Farkas, T., Daugaard, M., & Jäättelä, M. (2011). Identification of Small Molecule
852 Inhibitors of Phosphatidylinositol 3-Kinase and Autophagy. *Journal of Biological*
853 *Chemistry*, *286*(45), 38904–38912. http://doi.org/10.1074/jbc.M111.269134
854 Fellmann, C., Hoffmann, T., Sridhar, V., Hopfgartner, B., Muhar, M., Roth, M., et al.
855 (2013). An Optimized microRNA Backbone for Effective Single-Copy RNAi.
856 *CellReports*, *5*(6), 1704–1713. http://doi.org/10.1016/j.celrep.2013.11.020
857 Foresti, O., Ruggiano, A., Hannibal-Bach, H. K., Ejsing, C. S., & Carvalho, P. (2013).
858 Sterol homeostasis requires regulated degradation of squalene monooxygenase by
859 the ubiquitin ligase Doa10/Teb4. *eLife*, *2*, 10189–17.
860 http://doi.org/10.7554/eLife.00953
861 Gao, R., Schellenberg, M. J., Huang, S.-Y. N., Abdelmalak, M., Marchand, C., Nitiss, K.
862 C., et al. (2014). Proteolytic degradation of topoisomerase II (Top2) enables the
863 processing of Top2·DNA and Top2·RNA covalent complexes by tyrosyl-DNA-
864 phosphodiesterase 2 (TDP2). *Journal of Biological Chemistry*, *289*(26), 17960–
865 17969. http://doi.org/10.1074/jbc.M114.565374

866 Guilluy, C., Osborne, L. D., Van Landeghem, L., Sharek, L., Superfine, R., Garcia-Mata,
867 R., & Burridge, K. (2014). Isolated nuclei adapt to force and reveal a
868 mechanotransduction pathway in the nucleus. *Nature Cell Biology*, *16*(4), 376–381.
869 http://doi.org/10.1038/ncb2927
870 Harding, H. P., Zhang, Y., & Ron, D. (1999). Protein translation and folding are coupled
871 by an endoplasmic-reticulum-resident kinase. *Nature*, *397*(6716), 271–274.
872 http://doi.org/10.1038/16729
873 He, L., Diedrich, J., Chu, Y.-Y., & Yates, J. R., III. (2015). Extracting Accurate Precursor
874 Information for Tandem Mass Spectra by RawConverter. *Analytical Chemistry*,
875 *87*(22), 11361–11367. http://doi.org/10.1021/acs.analchem.5b02721
876 Heckman, K. L., & Pease, L. R. (2007). Gene splicing and mutagenesis by PCR-driven
877 overlap extension. *Nature Protocols*, *2*(4), 924–932.
878 http://doi.org/10.1038/nprot.2007.132
879 Hegde, R. S., & Zavodszky, E. (2019). Recognition and Degradation of Mislocalized
880 Proteins in Health and Disease. *Cold Spring Harbor Perspectives in Biology*,
881 a033902–19. http://doi.org/10.1101/cshperspect.a033902
882 Hofemeister, H., & O'Hare, P. (2005). Analysis of the Localization and Topology of
883 Nurim, a Polytopic Protein Tightly Associated with the Inner Nuclear Membrane.
884 *Journal of Biological Chemistry*, *280*(4), 2512–2521.
885 http://doi.org/10.1074/jbc.M410504200
886 Katta, S. S., Smoyer, C. J., & Jaspersen, S. L. (2014). Destination: inner nuclear
887 membrane. *Trends in Cell Biology*, *24*(4), 221–229.
888 http://doi.org/10.1016/j.tcb.2013.10.006
889 Khmelinskii, A., Blaszczak, E., Pantazopoulou, M., Fischer, B., Omnus, D. J., Le Dez,
890 G., Brossard, A., Gunnarsson, A., Barry, J. D., Meurer, M., Kirrmaier, D., Boone, C.,
891 Huber, W., Rabut, G., Ljungdahl, P. O., & Knop, M. (2014a). Protein quality control
892 at the inner nuclear membrane. *Nature*, *516*(7531), 410–413.
893 http://doi.org/10.1038/nature14096
894 Khmelinskii, A., Blaszczak, E., Pantazopoulou, M., Fischer, B., Omnus, D. J., Le Dez,
895 G., Brossard, A., Gunnarsson, A., Barry, J. D., Meurer, M., Kirrmaier, D., Boone, C.,
896 Huber, W., Rabut, G., Ljungdahl, P. O., & Knop, M. (2014b). Protein quality control

897 at the inner nuclear membrane. *Nature*, *516*(7531), 410–413.
898 http://doi.org/10.1038/nature14096
899 Klionsky, D. J., Abdelmohsen, K., Abe, A., Abedin, M. J., Abeliovich, H., Arozena, A. A.,
900 et al. (2016). Guidelines for the use and interpretation of assays for monitoring
901 autophagy \(3rd edition\). *Autophagy*, *12*(1), 1–222.
902 http://doi.org/10.1080/15548627.2015.1100356
903 Krogh, A., Larsson, B., Heijne, von, G., & Sonnhammer, E. L. L. (2001). Predicting
904 transmembrane protein topology with a hidden markov model: application to
905 complete genomes11Edited by F. Cohen. *Journal of Molecular Biology*, *305*(3),
906 567–580. http://doi.org/10.1006/jmbi.2000.4315
907 Leto, D. E., Morgens, D. W., Zhang, L., Walczak, C. P., Elias, J. E., Bassik, M. C., &
908 Kopito, R. R. (2019). Genome-wide CRISPR Analysis Identifies Substrate- Specific
909 Conjugation Modules in ER-Associated Degradation. *Molecular Cell*, *73*(2), 377–
910 389.e11. http://doi.org/10.1016/j.molcel.2018.11.015
911 Ong, S.-E., & Mann, M. (2007). A practical recipe for stable isotope labeling by amino
912 acids in cell culture (SILAC). *Nature Protocols*, *1*(6), 2650–2660.
913 http://doi.org/10.1038/nprot.2006.427
914 Park, S. K. R., Aslanian, A., McClatchy, D. B., Han, X., Shah, H., Singh, M., et al.
915 (2014). Census 2: isobaric labeling data analysis. *Bioinformatics (Oxford, England)*,
916 *30*(15), 2208–2209. http://doi.org/10.1093/bioinformatics/btu151
917 Pryszcz, L. P., Huerta-Cepas, J., & Gabaldón, T. (2010). MetaPhOrs: orthology and
918 paralogy predictions from multiple phylogenetic evidence using a consistency-based
919 confidence score. *Nucleic Acids Research*, *39*(5), e32–e32.
920 http://doi.org/10.1093/nar/gkq953
921 Rolls, M. M., Stein, P. A., Taylor, S. S., Ha, E., McKeon, F., & Rapoport, T. A. (1999). A
922 Visual Screen of a Gfp-Fusion Library Identifies a New Type of Nuclear Envelope
923 Membrane Protein. *The Journal of Cell Biology*, *146*(1), 29–44.
924 http://doi.org/10.1083/jcb.146.1.29
925 Ruggiano, A., Foresti, O., & Carvalho, P. (2014). ER-associated degradation: Protein
926 quality control and beyond. *The Journal of Cell Biology*, *204*(6), 869–879.
927 http://doi.org/10.1083/jcb.201312042

928 Saftig, P., & Klumperman, J. (2009). Lysosome biogenesis and lysosomal membrane
929 proteins: trafficking meets function, 1–13. http://doi.org/10.1038/nrm2745
930 Satpute-Krishnan, P., Ajinkya, M., Bhat, S., Itakura, E., Hegde, R. S., & Lippincott-
931 Schwartz, J. (2014). ER Stress-Induced Clearance of Misfolded GPI-Anchored
932 Proteins via the Secretory Pathway. *Cell*, *158*(3), 522–533.
933 http://doi.org/10.1016/j.cell.2014.06.026
934 Schirmer, E. C., Florens, L., Guan, T., Yates, J. R., & Gerace, L. (2003). Nuclear
935 membrane proteins with potential disease links found by subtractive proteomics.
936 *Science*, *301*(5638), 1380–1382. http://doi.org/10.1126/science.1088176
937 Schreiber, K. H., & Kennedy, B. K. (2013). When Lamins Go Bad: Nuclear Structure
938 and Disease. *Cell*, *152*(6), 1365–1375. http://doi.org/10.1016/j.cell.2013.02.015
939 Shimi, T., Koujin, T., Segura-Totten, M., Wilson, K. L., Haraguchi, T., & Hiraoka, Y.
940 (2004). Dynamic interaction between BAF and emerin revealed by FRAP, FLIP, and
941 FRET analyses in living HeLa cells. *Journal of Structural Biology*, *147*(1), 31–41.
942 http://doi.org/10.1016/j.jsb.2003.11.013
943 Smith, M. D., Harley, M. E., Kemp, A. J., Wills, J., Lee, M., Arends, M., et al. (2018).
944 CCPG1 Is a Non-canonical Autophagy Cargo Receptor Essential for ER-Phagy and
945 Pancreatic ER Proteostasis. *Developmental Cell*, *44*(2), 217–232.e11.
946 http://doi.org/10.1016/j.devcel.2017.11.024
947 Tabb, D. L., McDonald, W. H., & Yates, J. R. (2002). DTASelect and Contrast: tools for
948 assembling and comparing protein identifications from shotgun proteomics. *Journal
949 of Proteome Research*, *1*(1), 21–26.
950 Toyama, B. H., Arrojo e Drigo, R., Lev-Ram, V., Ramachandra, R., Deerinck, T. J.,
951 Lechene, C., et al. (2019). Visualization of long-lived proteins reveals age
952 mosaicism within nuclei of postmitotic cells. *The Journal of Cell Biology*, *218*(2),
953 433–444. http://doi.org/10.1083/jcb.201809123
954 Toyama, B. H., Savas, J. N., Park, S. K., Harris, M. S., Ingolia, N. T., Yates, J. R., III, &
955 Hetzer, M. W. (2013). Identification of Long-Lived Proteins Reveals Exceptional
956 Stability of Essential Cellular Structures. *Cell*, *154*(5), 971–982.
957 http://doi.org/10.1016/j.cell.2013.07.037

958 Tsai, P.-L., Zhao, C., Turner, E., & Schlieker, C. (2016). The Lamin B receptor is
959 essential for cholesterol synthesis and perturbed by disease-causing mutations.
960 *eLife*, *5*, 4181. http://doi.org/10.7554/eLife.16011
961 Uhlen, M., Fagerberg, L., Hallstrom, B. M., Lindskog, C., Oksvold, P., Mardinoglu, A., et
962 al. (2015). Tissue-based map of the human proteome. *Science*, *347*(6220),
963 1260419–1260419. http://doi.org/10.1126/science.1260419
964 Ungricht, R., Klann, M., Horvath, P., & Kutay, U. (2015). Diffusion and retention are
965 major determinants of protein targeting to the inner nuclear membrane. *The Journal*
966 *of Cell Biology*, *209*(5), 687–704. http://doi.org/10.1083/jcb.201409127
967 Vaughan, A., Alvarez-Reyes, M., Bridger, J. M., Broers, J. L., Ramaekers, F. C.,
968 Wehnert, M., et al. (2001). Both emerin and lamin C depend on lamin A for
969 localization at the nuclear envelope. *Journal of Cell Science*, *114*(Pt 14), 2577–
970 2590.
971 Verzijlbergen, K. F., Menendez-Benito, V., van Welsem, T., van Deventer, S. J.,
972 Lindstrom, D. L., Ovaa, H., et al. (2010). Recombination-induced tag exchange to
973 track old and new proteins. *Proceedings of the National Academy of Sciences*,
974 *107*(1), 64–68. http://doi.org/10.1073/pnas.0911164107
975 Wang, Q., Li, L., & Ye, Y. (2008). Inhibition of p97-dependent Protein Degradation by
976 Eeyarestatin I. *Journal of Biological Chemistry*, *283*(12), 7445–7454.
977 http://doi.org/10.1074/jbc.M708347200
978 Xu, T., Park, S. K., Venable, J. D., Wohlschlegel, J. A., Diedrich, J. K., Cociorva, D., et
979 al. (2015). ProLuCID: An improved SEQUEST-like algorithm with enhanced
980 sensitivity and specificity. *Journal of Proteomics*, *129*(C), 16–24.
981 http://doi.org/10.1016/j.jprot.2015.07.001
982 Zattas, D., Berk, J. M., Kreft, S. G., & Hochstrasser, M. (2016). A Conserved C-terminal
983 Element in the Yeast Doa10 and Human MARCH6 Ubiquitin Ligases Required for
984 Selective Substrate Degradation. *Journal of Biological Chemistry*, *291*(23), 12105–
985 12118. http://doi.org/10.1074/jbc.M116.726877
986 Zhang, K., Sha, J., & Harter, M. L. (2010). Activation of Cdc6 by MyoD is associated
987 with the expansion of quiescent myogenic satellite cells. *The Journal of Cell Biology*,
988 *188*(1), 39–48. http://doi.org/10.1083/jcb.200904144

Figure S1. Half life fit examples

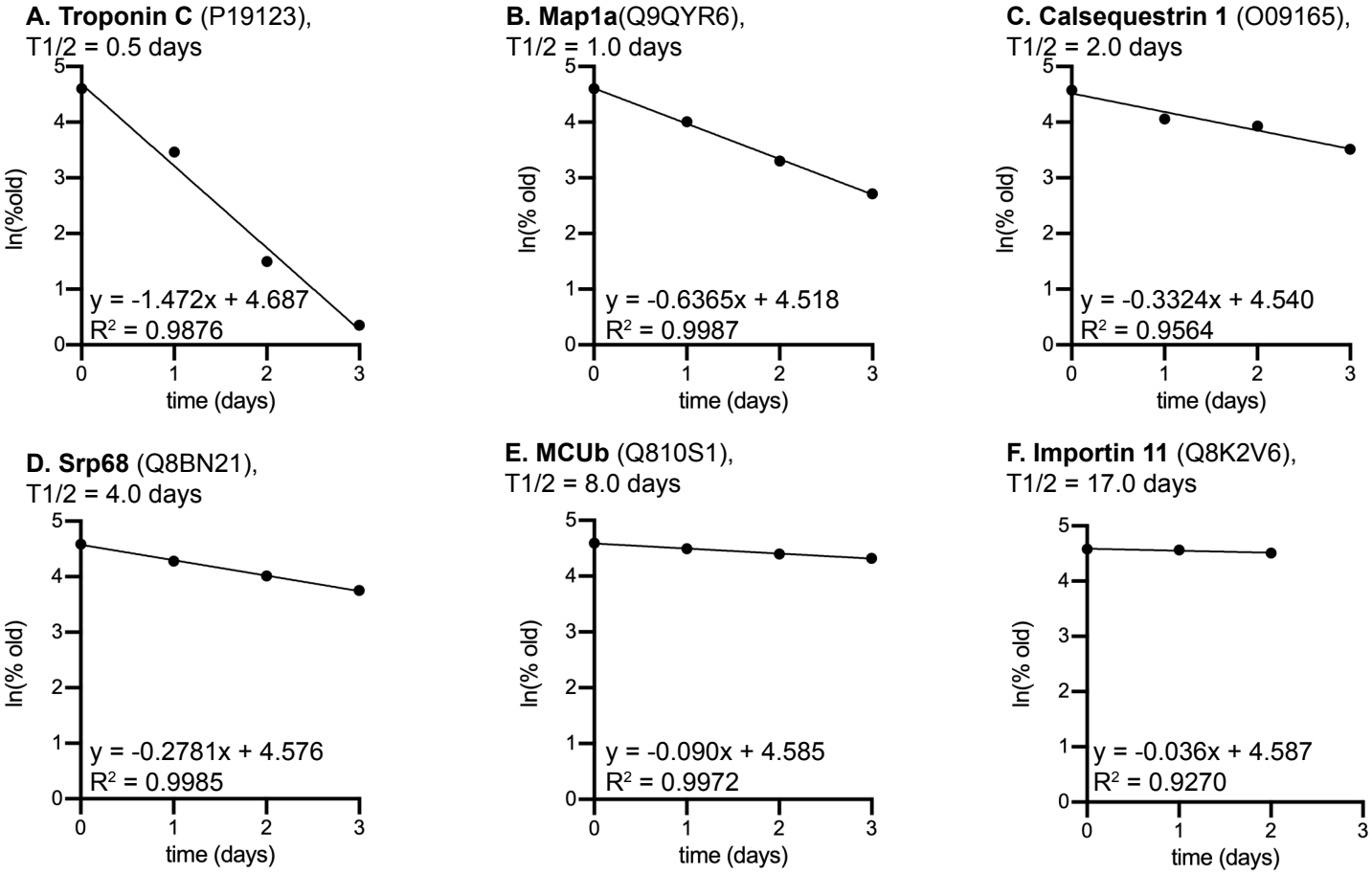

Figure S2. Identification of a disease-linked emerin mutant with normal localization and NE residence time

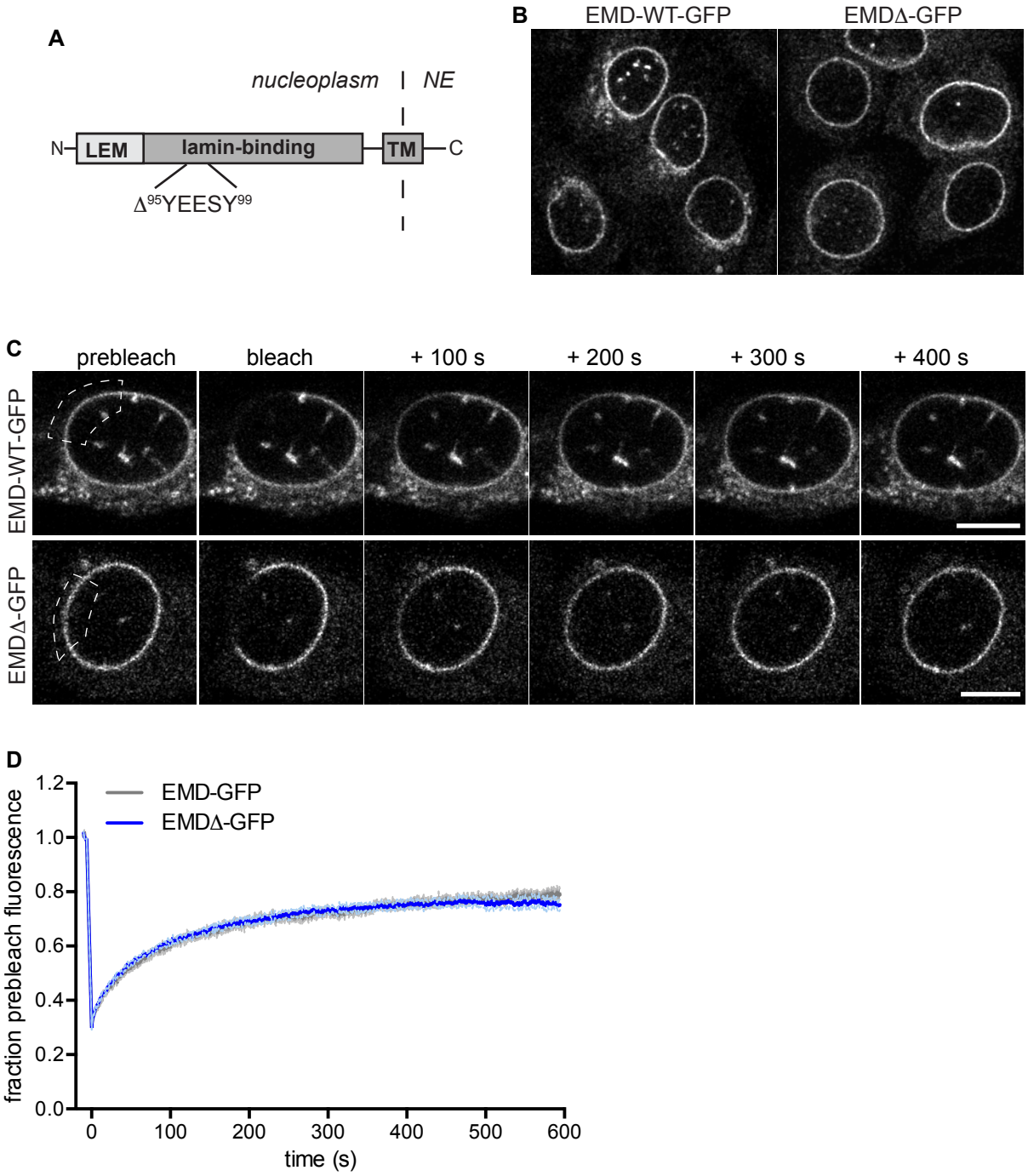

Figure S3. Accumulation of non-membrane-associated higher molecular weight EMD species upon proteasome inhibition

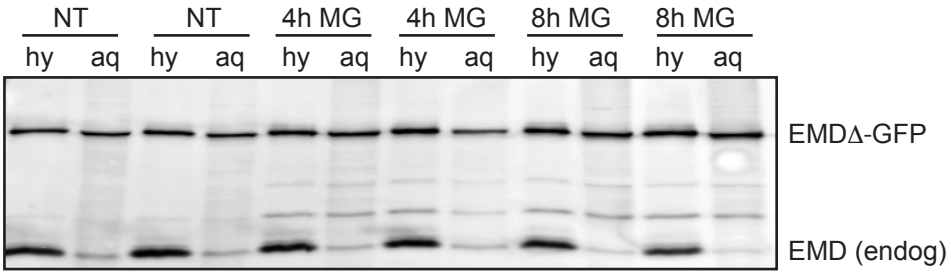

Figure S4. siRNA-mediated E2 or E3 ubiquitin ligase knockdowns do not stabilize emerin variants.

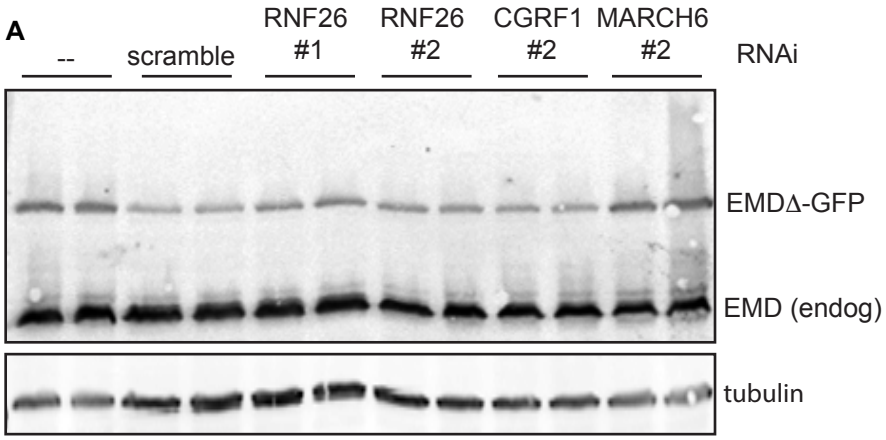

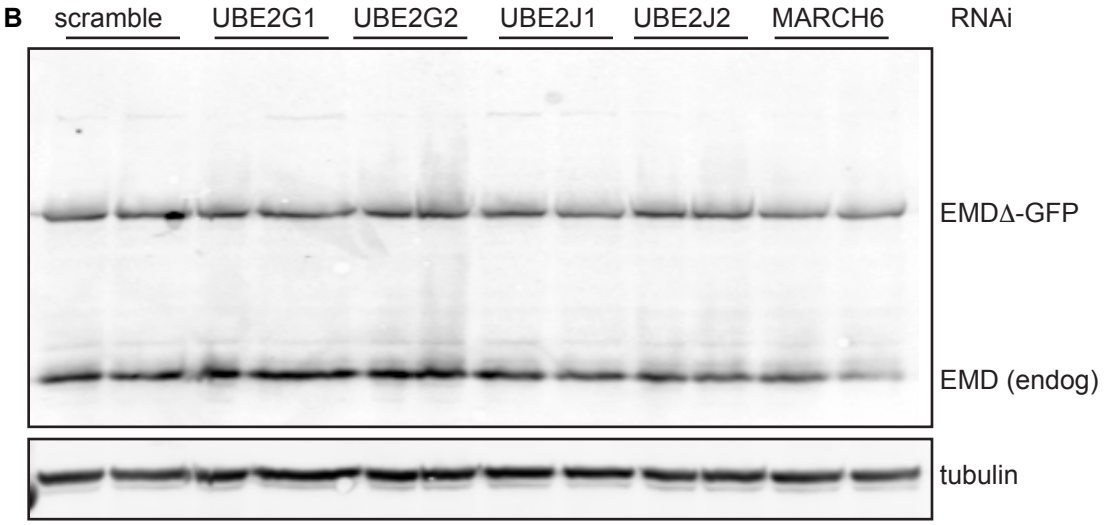

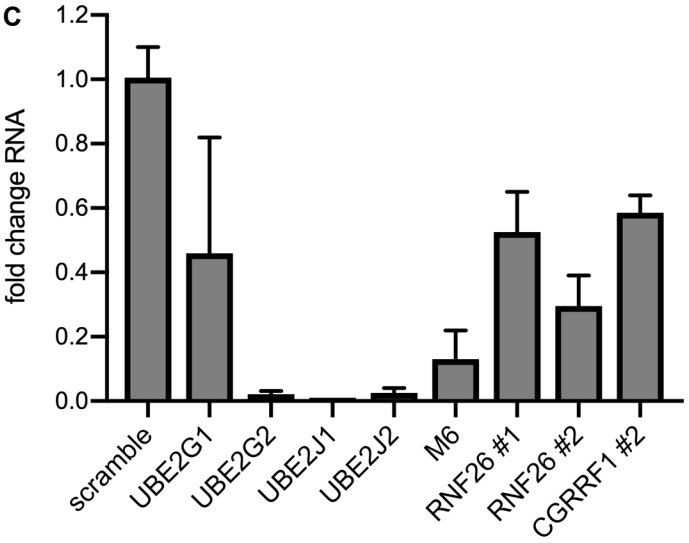

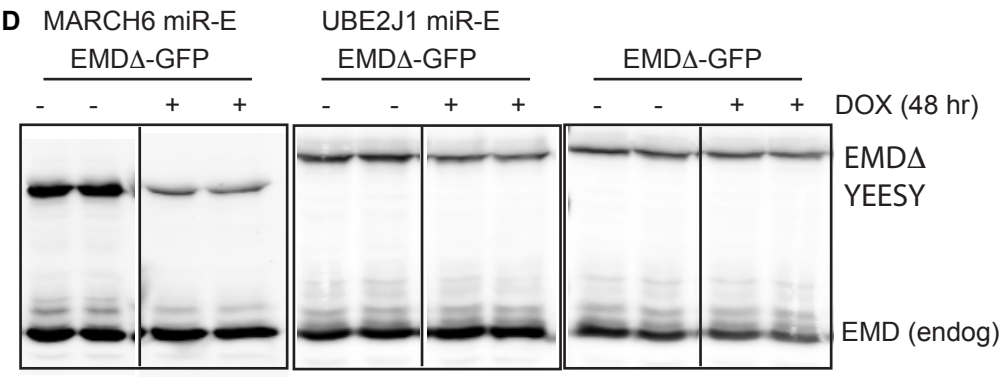

Figure S5. emerin is mislocalized to the ER but not degraded in lmna -/- MEFs.

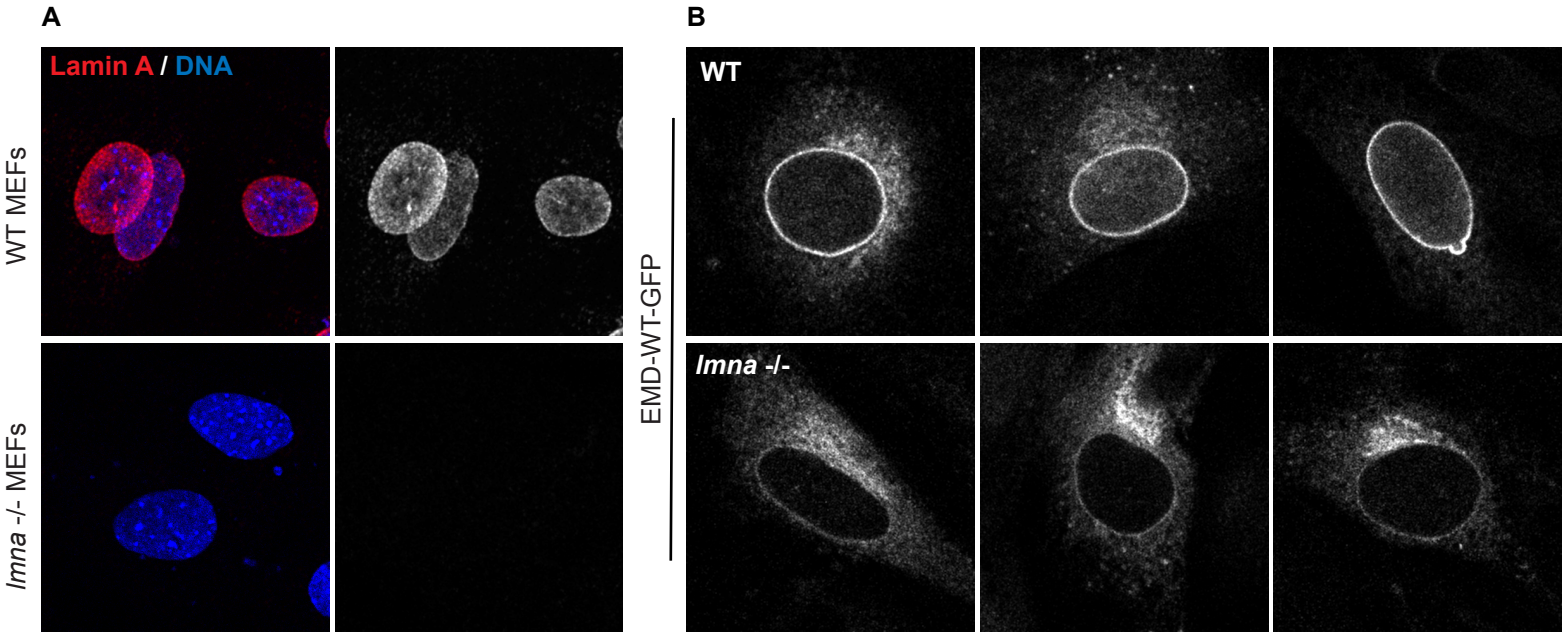

Supplemental Figure Legends

Figure S1. Examples of half-life fits for proteins with predicted half-lives of 0.5 days (A), 1 day (B), 2 days (C), 4 days (D), 8 days (E), and 17 days (F).

Figure S2. Identification of a disease-linked emerin variant (A) with normal localization (B) and normal residence time at the NE (C,D).

Figure S3. Accumulation of non-membrane-associated higher molecular weight EMD species upon proteasome inhibition. C2C12 cells stably expressing EMDΔ-GFP were treated with proteasome inhibitor (MG132) for the indicated times, then subjected to Triton-X-114 fractionation to separate hydrophobic/membrane-associated proteins from hydrophilic/soluble proteins. Anti-EMD antibody was used to detect endogenous EMD (mostly hydrophobic) and exogenous EMDΔ-GFP, which is present in both fractions and accumulates in higher molecular weight, soluble species upon proteasome inhibition.

Figure S4. siRNA-mediated E2 ubiquitin-conjugating enzyme or E3 ubiquitin ligase knockdowns do not stabilize emerin variants. (A-B) EMDΔ-GFP protein levels do not change in C2C12 cells stably expressing EMDΔ-GFP that were transfected in duplicate with 50 nM RNAi targeting the E3 ubiquitin ligases Rnf26, CGRRF1, MARCH6, or a scrambled control (A), or targeting the E2 ubiquitin conjugating enzymes UBE2G1, UBE2G2, UBE2J1, and UBE2J2 (B). (C) qPCR quantification of RNAi knockdown efficiency for conditions shown in (A-B). (D) EMDΔ-GFP protein levels either decrease or do not change in U2OS cells stably expressing EMDΔ-GFP and induced to express a miR-E RNAi cassette targeting the E3 ubiquitin ligase MARCH6 or the E2 ubiquitin conjugating enzyme UBE2J1 for 48 hours.

Figure S5. Emerin is mislocalized to the ER, but not degraded in *lmna -/-* MEFs. (A) representative immunostaining of WT MEFs or of *lmna -/-* MEFs with lamin A antibody (red) and Hoechst (blue). (B) Representative immunofluorescence of EMD-GFP stably expressed in WT MEFs (top panel) or *lmna -/-* MEFs (bottom panel).